POLITECNICO DI TORINO
Repository ISTITUZIONALE

Mediterranean offshore wind spatial potential: focusing on national target of Italy, Greece and Cyprus for electricity and hydrogen production

Original
Mediterranean offshore wind spatial potential: focusing on national target of Italy, Greece and Cyprus for electricity and hydrogen production / Petracca, E., De Clerck, V., Gorr-Pozzi, E., Mangia, G., Haider Joyo, F., Francisco Marques, J., Bracco, G.. - In: RENEWABLE ENERGY. - ISSN 1879-0682. - 279:(2026). [10.1016/j.renene.2026.126575]

Availability:
This version is available at: 11583/3017614 since: 2026-11-06T10:16:27Z

Publisher:
Elsevier

Published
DOI:10.1016/j.renene.2026.126575

Terms of use:

This article is made available under terms and conditions as specified in the corresponding bibliographic description in the repository

Publisher copyright

(Article begins on next page)

10 November 2026

Renewable Energy 279 (2026) 126575

Contents lists available at ScienceDirect

Renewable Energy

journal homepage: www.elsevier.com/locate/renene

Mediterranean offshore wind spatial potential: Focusing on national targets of Italy, Greece and Cyprus for electricity and hydrogen production

Ermando Petracca [a], Viola De Clerck [a], Emiliano Gorr-Pozzi [a,*], Gabriele Mangia [a], Farhan Haider Joyo [b], João Francisco Marques [c], Giovanni Bracco [a]

[a] Marine Offshore Renewable Energy Lab (MOREnergy Lab), Department of Mechanical and Aerospace Engineering, Politecnico di Torino, Corso Duca degli Abruzzi 24, 10129, Torino, Italy
[b] Department of Electrical and Energy Engineering, Sapienza University of Rome, Via Eudossiana 18, 00184, Rome, Italy
[c] EDP NEW, Avenida 24 de Julho 12, 1249-300, Lisbon, Portugal

ARTICLE INFO

Keywords:
Floating offshore wind
Geospatial analysis (GIS)
Mediterranean sea
Levelised cost of energy (LCOE)
Power-to-X (P2X)

ABSTRACT

Offshore wind and green hydrogen are expected to play a central role in Mediterranean decarbonisation, yet deep waters, intense coastal uses, and visual-acceptance constraints make siting and system design challenging. This study develops an integrated geospatial and techno-economic framework that combines marine spatial-planning layers, long-term wind reanalysis, offshore wind-farm design, and power-to-x valuation to assess where offshore wind can support electricity supply and hydrogen production. Spatial exclusions, bathymetric limits, and a visual-impact index reduce the basin to about $6.6 \cdot 10^5$ km^2 of eligible sea space (about 24% of the Mediterranean). For each grid cell, multi-year wind series are coupled with precomputed performance and cost tables for fixed-bottom and floating concepts, multiple turbine ratings, layouts, and spacings, producing spatially resolved indicators for annual electricity yield and levelised costs for electricity and hydrogen. For Italy, Greece, and Cyprus, 2030 electricity and hydrogen targets can be met using less than 8% of the eligible area, while export-oriented 2050 cases require up to about 55% in Italy and 75% in Greece and Cyprus, with avoided emissions on the order of several tens of $MtCO_2\ yr^{-1}$.

1. Introduction

Mediterranean decarbonisation pathways increasingly identify offshore wind as a renewable-energy source, with EU and regional targets promoting large-scale deployment for mid-century CO_2 abatement [1]. Compared with onshore installations in densely populated coastal regions, offshore wind can access stronger and more stable wind resources, improving energy yield and potentially reducing the levelised cost of energy (LCOE). However, unlike mature basins such as the North Sea, the Mediterranean is characterised by steep bathymetry and deep waters close to shore, limiting bottom-fixed deployment and favouring floating offshore wind turbines (FOWTs) [2]. Although floating technologies unlock large deep-water resources, they involve higher installation and maintenance costs. In addition, offshore wind production remains variable and affected by wake losses, particularly under stable atmospheric conditions [3]. Large-scale offshore integration may increase congestion, curtailment, and revenue volatility, reinforcing the need for flexibility and sector-coupling solutions.

Among Power-to-X (PtX) pathways, hydrogen is emerging as a key energy carrier, while production remains largely fossil-based [4]. In the Mediterranean, where offshore renewable resources are substantial but grid expansion and coastal land availability remain constrained, PtX solutions can help valorise offshore wind potential while mitigating curtailment and congestion issues. Offshore wind-to-hydrogen concepts are also being considered for the Mediterranean, highlighting growing interest in coupling floating wind farms with electrolysis [4]. A central design question concerns the siting of electrolysers, either onshore near demand centres or offshore in PtX hubs co-located with large wind farms. Studies suggest that offshore hydrogen production could become cost-competitive beyond 2030 as declining electrolyser and platform costs partly offset the added complexity of offshore systems [4]. Addressing the environmental [5], regulatory, and spatial constraints of Mediterranean offshore wind development therefore requires integrated regional-scale assessment methodologies combining marine spatial planning (MSP), high-resolution metocean data, offshore wind-farm design, and PtX valuation [6].

Offshore wind planning has been analysed through geospatial and techno-economic approaches combining wind-resource assessment, exclusion criteria, and cost models. For the Mediterranean, Faraggiana

* Corresponding author.
E-mail address: emiliano.gorr@polito.it (E. Gorr-Pozzi).

https://doi.org/10.1016/j.renene.2026.126575
Received 18 July 2026; Received in revised form 1 October 2026; Accepted 13 October 2026
Available online 27 October 2026
0960-1481/© 2026 The Authors. Published by Elsevier Ltd. This is an open access article under the CC BY license (http://creativecommons.org/licenses/by/4.0/).

et al. estimate an optimised floating technical capacity of 782 GW, with an average capacity factor of 31.8% and an average LCOE of 93.4 €MWh^{-1}, mainly concentrated in Libya, Tunisia, Italy, and Greece [7]. Complementing these bottom-up assessments, the "Study on the offshore grid potential in the Mediterranean region" estimates a technical offshore wind potential of about 90–125 GW by 2050 for the analysed Mediterranean countries, focusing on export corridors and meshed-grid concepts rather than detailed farm layouts [8]. More recent developments have integrated bathymetry, maintenance accessibility, wave climate, and infrastructure availability into regional-scale offshore wind assessments. For Italy and the wider Mediterranean, Serri et al. review the technical and economic challenges of floating offshore wind deployment, emphasising the combined influence of deep-water conditions, infrastructure, and regional constraints [9]. However, MSP and environmental constraints remain only partially integrated into GIS-based offshore wind studies [10].

Despite recent progress, Mediterranean-scale assessments still rely on simplified offshore wind-farm representations to maintain basin-scale tractability [7]. Fixed layouts, simplified electrical topologies, and aggregated cost assumptions may inadequately capture the strong site-specific constraints imposed by Mediterranean bathymetry, limited shelf areas, and fragmented maritime boundaries. In addition, large-scale studies commonly adopt generic turbine-performance and wake-loss assumptions, introducing uncertainty in location-specific energy yield and techno-economic comparisons. Social constraints are also frequently represented through simplified distance-to-shore buffers, without explicitly accounting for visibility impacts. For offshore wind-to-hydrogen systems, recent studies mainly focus on techno-economic analyses of specific project configurations. Travaglini et al. [11] analyse a floating wind farm in the western Mediterranean where electrolysis is supplied exclusively by curtailed power, reporting LCOH values of about 3.8-5.5 €/kg for 10 and 15 MW turbines under a fixed radial layout. Jiang et al. [12] compare onshore, offshore distributed, and offshore centralised hydrogen-production pathways, showing that increasing distance to shore and hydrogen transport requirements can shift the least-cost solution from onshore to offshore production. However, these studies generally rely on stylised project-scale configurations and rarely integrate basin-wide spatial constraints, marine competing uses, and offshore wind suitability within a unified framework. At the same time, geospatial offshore wind assessments seldom propagate spatially resolved LCOE results into hydrogen-oriented metrics such as LCOH.

1.1. Identified research gaps

Existing literature therefore remains fragmented between basin-scale offshore wind assessments and project-scale offshore hydrogen analyses. Geospatial studies typically evaluate offshore wind potential and LCOE under simplified design assumptions, while offshore hydrogen studies rarely include explicit MSP constraints, detailed wind-farm optimisation, or visual-impact assessment. In particular, farm layout, internal electrical topology, and floating versus bottom-fixed concepts are generally decoupled from basin-scale spatial screening. This work develops a Mediterranean-wide geospatial and techno-economic methodology coupling MSP constraints, wind-resource assessment, offshore wind-farm optimisation, visual-impact screening, and hydrogen-production modelling. A full techno-economic optimisation of spacing, turbine size, foundation type, and internal electrical layout is performed for each eligible grid cell. The resulting LCOE maps are then integrated into a wind-to-hydrogen chain to compute LCOH, offshore-area utilisation, coverage ratios for national offshore-wind and hydrogen targets, and associated CO_2 abatement for Italy, Greece, and Cyprus.

The paper is organised as follows: Section 2 describes the geospatial screening, wind-farm and PtX modelling, and scenario definition; Section 3 presents the basin-wide technical potential, optimal layouts, and techno-economic results; Section 4 discusses the results in the context of previous Mediterranean assessments; and Section 5 summarises the main findings and future developments.

2. Material and methodology

2.1. Geospatial analysis

Fig. 1 summarises the overall workflow of the proposed methodology. Starting from MSP-constrained eligible areas and long-term wind time series, the framework first estimates the maximum installable offshore wind capacity and the associated annual electricity production. In a second step, alternative Power-to-X scenarios are investigated, in which the extracted power is either delivered to the grid or converted into green hydrogen, allowing the equivalent H_2 production and the associated techno-economic indicators to be quantified, namely the LCOE and the LCOH. The model is applied to a wide range of offshore wind technology and design scenarios, encompassing both fixed-bottom and floating wind farms, as well as different turbine rating classes. Multiple foundation concepts, wind farm scales, array densities, and internal electrical layouts are considered in order to capture the impact of design choices on energy production, losses, and costs. Both high-voltage alternating current (HVAC) and high-voltage direct current (HVDC) export solutions are included to account for transmission-related losses and costs as a function of distance to shore and installed capacity. Wind farm productivity is evaluated from directional wind speed time series, explicitly accounting for aerodynamic wake interactions and electrical losses within the internal and export grids.

The GIS workflow, input datasets, coordinate reference system and cell-area calculation follow the framework described in [13]. Overlapping exclusion layers are combined into a single eligibility mask, while EEZ boundaries are used for country-level attribution of the final eligible cells.

2.2. Eligible area identification

The identification of eligible areas is a crucial step, as it ensures both the technical feasibility of offshore wind farm installations and the systematic consideration of human activities and exclusion zones. Following the approach in [8], spatial constraints related to military zones, marine protected areas, high-traffic shipping routes, and Exclusive Economic Zones (EEZs) are derived from the European Marine Observation and Data Network (EMODnet) [14]. Bathymetric constraints are subsequently imposed using data from the General Bathymetric Chart of the Oceans (GEBCO) [15]. These layers are used to apply technology-specific depth limits for the wind turbines considered. In this work, sea cells eligible for offshore wind deployment are identified by applying technology-specific constraints: fixed-bottom wind turbines are regarded for water depths between 20 m and 60 m, while floating wind turbines are analysed for water depths ranging from 60 m to 1000 m and are required to be located at least 12 km from the coastline to account for visual-impact constraints, and are retained as eligible for offshore wind deployment. The resulting eligibility mask should therefore be interpreted as a basin-scale, static screening layer based on currently available geospatial constraints, rather than as a permitting-level assessment of site-specific trade-offs among environmental protection, maritime uses, and offshore energy development.

2.3. Spatially annual energy production and annual hydrogen production

2.3.1. Annual energy production

To estimate the annual energy production (AEP), a dedicated simulation framework is developed that couples detailed technical modelling with wind-resource data, following and extending the approach of [7]. The framework is applied to a wide range of offshore wind farm configurations, including both fixed-bottom and floating technologies, and turbine rated capacities of 10 MW and 15 MW. The reference turbine models are the DTU 10 MW [16] and the IEA 15 MW [17]. Fixed-bottom turbines are modelled with monopile foundations, while

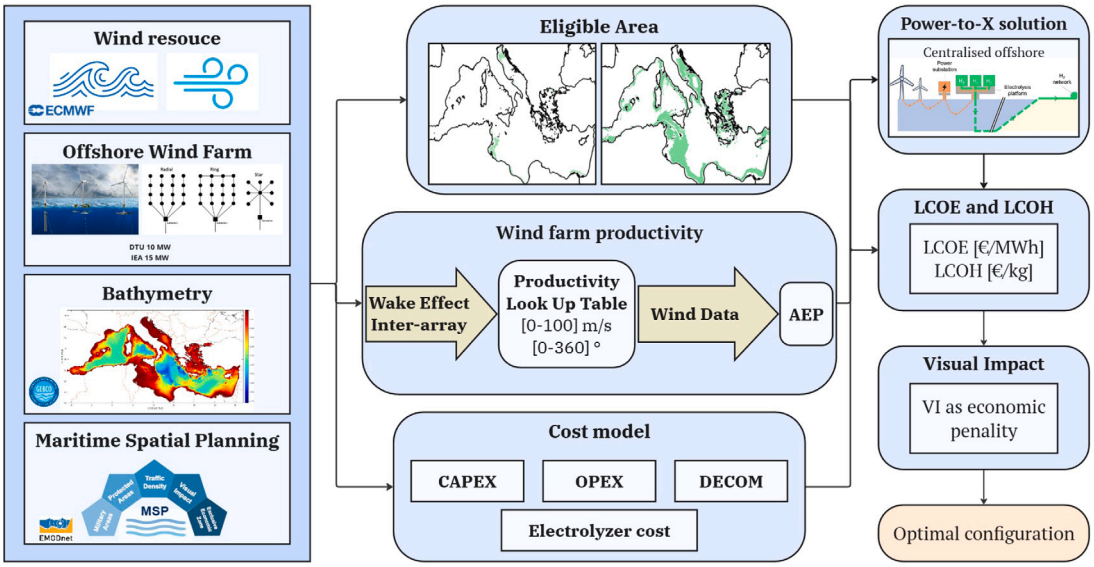


Fig. 1. Workflow of the proposed methodology.

floating configurations include semi-submersible, spar, and tension-leg platform (TLP) substructures. For fixed-bottom turbines, the reference power curve is adopted. For floating turbines, power curves are modified to account for performance losses induced by platform motion. These losses are evaluated by modelling the hydrodynamic interaction between the floating substructure and the sea state using the MOST tool [18]. For each configuration, productivity look-up tables are generated considering three wind farm sizes (0.99 GW, 1.5 GW, and 3 GW), three internal electrical layouts (radial, star, and double-ring), and seven inter-turbine spacings, capturing wake interactions across a broad range of array densities. The selected ratings represent utility-scale design cases spanning approximately 1 GW to multi-GW offshore developments. They are exactly compatible with both turbine classes considered: 0.99 GW corresponds to 99 turbines of 10 MW or 66 turbines of 15 MW; 1.5 GW corresponds to 150 or 100 turbines, respectively; and 3 GW corresponds to 300 or 200 turbines, respectively. This enables a consistent comparison of layouts and spacings while capturing the non-linear scaling of farm footprint, wake losses, and electrical infrastructure. The selected ratings are therefore modelling cases, rather than projections of individual permitted projects.

An illustrative example of the resulting wind-farm layout and internal electrical topology is shown in Fig. 2, where the number of turbines is reduced for clarity.

Look-up tables are computed on a grid of 1001 wind speeds (0–100 m/s) and 361 wind directions (0-360°), using power curves corrected for wake-induced velocity deficits and internal electrical losses. Wind-resource data are taken from the Copernicus European Regional Reanalysis (CERRA) dataset [19], covering the period 2001–2020. CERRA provides wind-speed time series at 100 m above sea level with 3 h temporal resolution and a native horizontal resolution of 5.5 km × 5.5 km. Hub-height wind speed is obtained at each grid cell using a logarithmic wind profile, consistent with [7]. The AEP at each candidate location is computed by mapping the CERRA wind-speed time series onto the corresponding productivity look-up tables. A technical availability factor η_{avail} of 95% is applied to account for planned and unplanned downtime [20]. External electrical losses are then included as a function of the distance to the nearest onshore substation, yielding the net annual energy yield.

The total annual productivity for each simulated year y is computed as

$$\text{AEP}_{y,\text{tot}} = \Delta t \sum_{i=1}^{N_{t,y}} \left[\eta_{\text{avail}} \sum_{j=1}^{N_{\text{turb}}} P_j(t_i) - P_{\text{el}}(t_i) \right], \tag{1}$$

where $N_{t,y}$ is the number of time steps in year y, N_{turb} the number of turbines, $P_j(t_i)$ the electrical power of turbine j at time t_i (including wake and inter-array cable losses), $P_{\text{el}}(t_i)$ the instantaneous export-cable losses, and Δt the time-step length. Therefore, $\text{AEP}_{y,\text{tot}}$ represents the total annual productivity of the yth simulated year.

The AEP model explicitly accounts for aerodynamic and electrical losses. Wake effects are modelled using the Jensen kinematic model with conical wake expansion, while electrical losses are evaluated for both inter-array and export cables. Cable electrical parameters are determined through a sizing module based on nominal transmitted power, enabling instantaneous loss calculations as a function of power flow [7]. The internal layouts considered reflect trade-offs between simplicity, cost, and redundancy: radial layouts minimise complexity and cost, whereas star and double-ring layouts increase robustness at the expense of higher design complexity.

Power export from each offshore substation is modelled using either HVAC or HVDC transmission, both operated at 220 kV. While HVAC is commonly adopted for shorter distances, HVDC becomes preferable for larger distances due to reduced transmission losses and reactive power constraints. Onshore high-voltage substation locations are identified following [8]. Each offshore site is assigned to its nearest onshore substation, allowing export-cable lengths to be determined consistently.

Finally, the cumulative nominal offshore wind capacity for each country is obtained by combining the total suitable area within national jurisdiction with the nominal power and spatial footprint of the reference wind-farm configuration selected as optimal at each location:

$$\text{Capacity}_{\text{nom,cum}}\ (\text{GW}) = P_{\text{farm,nom}} \cdot \frac{A_{\text{suitable}}}{A_{\text{farm}}}, \tag{2}$$

where $P_{\text{farm,nom}}$ [GW farm^{-1}] is the nominal (nameplate) power of one reference wind farm, A_{suitable} [km^2] is the eligible sea area, and A_{farm} [km^2 farm^{-1}] is the spatial footprint of one reference wind farm. The ratio $A_{\text{suitable}}/A_{\text{farm}}$ represents the number of equivalent wind farms that can be accommodated in the eligible area. Where the optimal configuration changes spatially, the capacity is evaluated cell by cell using the corresponding $P_{\text{farm,nom}}$ and A_{farm} values and subsequently summed.

2.3.2. Annual hydrogen production

To convert wind-generated electricity into hydrogen, a water electrolyser is required. Among available technologies, a proton-exchange membrane (PEM) electrolyser is adopted due to its favourable dynamic behaviour, including fast start-up, high permissible power-ramp

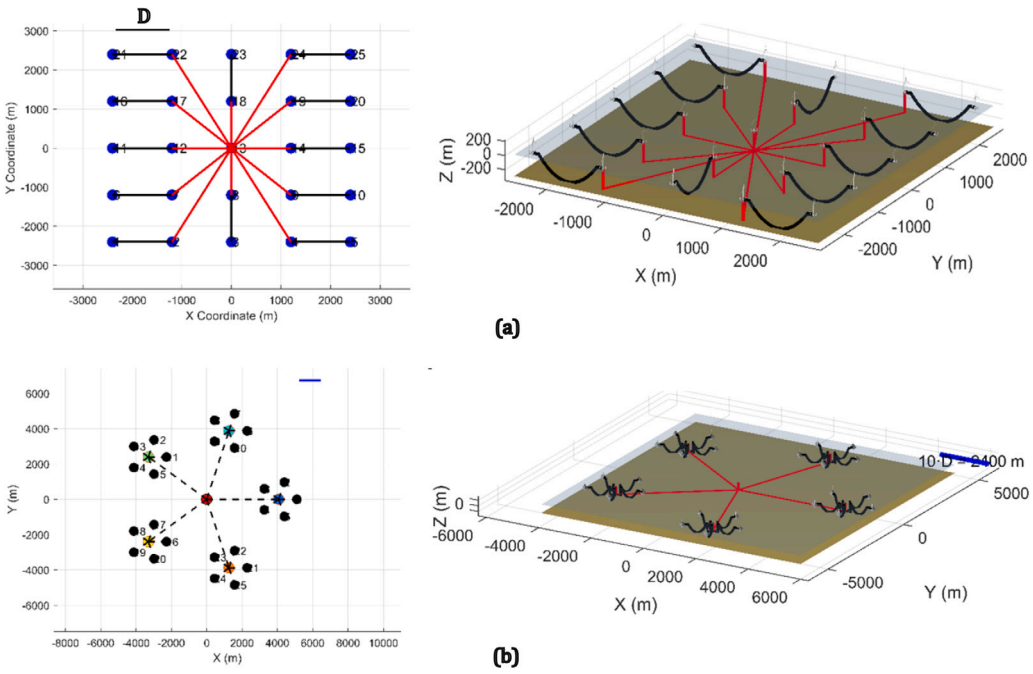


Fig. 2. Example wind-farm layout and internal electrical topology used in the optimisation. The number of turbines is reduced solely for visual clarity: (a) plan and 3D views of a radial collection system; (b) example of clustered strings and reduced-size farm layout.

rates, good part-load operation, high current densities, compact design, high hydrogen purity (> 99.8 %), short-term overload capability, and high outlet pressures. These advantages come at the expense of higher specific CAPEX and shorter stack lifetime compared to alkaline electrolysers [21]. Electrolyser performance is represented through a surrogate system-efficiency curve $\eta_{\mathrm{sys}}(P_{\mathrm{in}})$ derived from detailed models and manufacturer data [22]. Operation is allowed only above 10% of rated power, assumed as the minimum start-up threshold.

At each simulation time step, the net electrical power delivered to the electrolyser, $P_{\mathrm{PEM}}(t_i)$, is mapped to the corresponding efficiency $\eta_{\mathrm{el}}\left(P_{\mathrm{PEM}}(t_i)\right)$ (Fig. 3), yielding the instantaneous hydrogen production. The annual hydrogen production for each simulated year y and eligible grid cell x is computed as

$$\mathrm{AHP}_{y,x}\ (\mathrm{kg}) = \Delta t \sum_{i=1}^{N_{t,y}} \left(\left[\eta_{\mathrm{avail}} \sum_{j=1}^{N_{\mathrm{turb}}} P_j(t_i) \right] \eta_{\mathrm{el}}\left(P_{\mathrm{PEM}}(t_i)\right) LHV \right), \tag{3}$$

where $N_{t,y}$ is the number of time steps in year y, N_{turb} the number of turbines, $P_j(t_i)$ the power output of turbine j at time t_i (including wake and inter-array cable losses), η_{avail} the technical availability, LHV the lower heating value (considered as 33.33 kWh kg^{-1}), and Δt the time-step length. Therefore, $\mathrm{AHP}_{y,x}$ represents the hydrogen production of the reference wind farm associated with grid cell x in the yth simulated year. Accordingly, $P_{\mathrm{PEM}}(t_i)$ represents the net electrical input to the PEM electrolyser, consistent with the AEP formulation.

The electrolyser is assumed to be installed offshore; therefore, only inter-array losses are included, while export-cable losses are excluded. A one-to-one sizing between electrolyser rated power and wind farm rated power is adopted, representing a conservative near-term configuration while allowing future extensions to offshore or hybrid PtX hubs. The desalination system is modelled as a parasitic load equal to 0.14% of the electrolyser electrical input [23].

Analogously to wind capacity scaling, the total annual hydrogen production at the country level for each simulated year y is obtained by scaling the spatial mean of the tile-level values by the number of equivalent reference wind farms:

$$M_{\mathrm{H_2},y}^{(c)} = \frac{A_{\mathrm{suitable}}^{(c)}}{A_{\mathrm{farm}}} \left(\frac{1}{N_c} \sum_{x=1}^{N_c} \mathrm{AHP}_{y,x} \right), \tag{4}$$

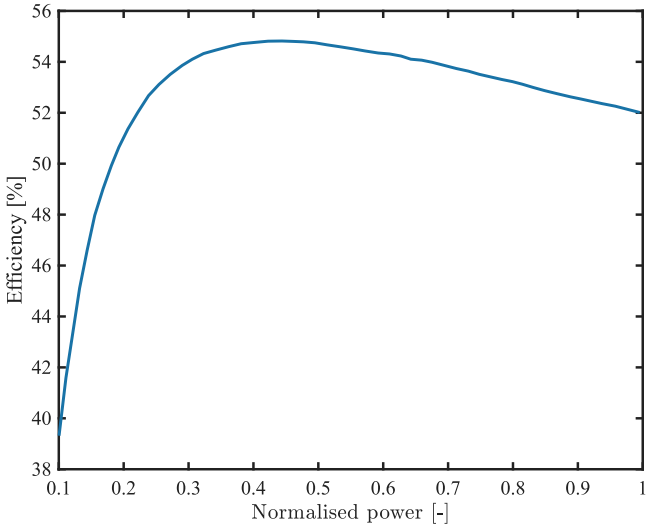


Fig. 3. Electrolyser efficiency as a function of normalised power.

where $A_{\mathrm{suitable}}^{(c)}$ is the available sea area within the national jurisdiction of country c, A_{farm} is the area occupied by one reference wind farm, and N_c is the number of eligible grid cells in that country. For equal-area tiles, the term in parentheses is the spatial mean of $\mathrm{AHP}_{y,x}$ across the eligible cells.

2.4. Economic performance metrics: LCOE and LCOH

The economic feasibility of the analysed configurations is evaluated through two main indicators: the LCOE for the offshore wind farm and the LCOH for the wind-to-hydrogen chain. In both cases, a discounted cash-flow model is used, accounting for CAPEX, operational expenditures (OPEX), and decommissioning costs (DECOM) over the entire project lifetime.

Table 1
Wind turbine and platform cost.

	Cost	Unit
10MW WT	10 933 182	€
15MW WT	1547 000	€/MW
Monopile	3601 003	€
Semi-Sub	750 000	€/MW
Spar	374 000	€/MW
TLP	93 450	€/MW

For the LCOE calculation, a weighted average cost of capital (WACC) of 8% and a project lifetime of 25 years are adopted, consistent with typical offshore-wind assumptions [24]. To reflect expected cost reductions towards 2030 and 2050, percentage-based adjustments are applied to the present-day CAPEX and OPEX: a 20% reduction is assumed for 2030 [25] and a 40% reduction for 2050 [26], in line with projections of declining LCOE driven by technological learning and supply-chain maturation for offshore wind and hydrogen technologies.

2.4.1. Capital expenditures

The total CAPEX of the offshore wind farm is decomposed into development, material, installation, and contingency costs:

$$\mathrm{CAPEX} = C_{\mathrm{DEV}} + C_{\mathrm{MAT}} + C_{\mathrm{INST}} + C_{\mathrm{CON}}, \tag{5}$$

where C_{DEV} denotes development costs, C_{MAT} component costs, C_{INST} installation costs, and C_{CON} contingency allowances.

The material cost is given by

$$C_{\mathrm{MAT}} = C_{\mathrm{FOWT}} + C_{\mathrm{mooring}} + C_{\mathrm{grid}}, \tag{6}$$

where C_{FOWT} includes turbines and floating platforms, C_{mooring} the mooring and anchoring system, and C_{grid} the electrical infrastructure.

Development costs cover permitting, environmental assessments, feasibility studies, and project preparation, and are modelled as a linear function of installed capacity with a unit cost of 0.17 M€/MW [27]. Turbine and platform costs for the considered turbine sizes and foundation types are reported in Table 1, based on [27–29].

Mooring-system costs C_{mooring} follow the methodology of [7], assuming drag-embedment anchors and parameterisation based on mooring-line length as a function of water depth. Electrical infrastructure costs comprise inter-array cable costs C_{int}, export cable costs C_{ex}, and onshore and offshore substation costs C_{Onsub}, and C_{Offsub}:

$$C_{\mathrm{grid}} = C_{\mathrm{int}} + C_{\mathrm{ex}} + C_{\mathrm{Offsub}} + C_{\mathrm{Onsub}}. \tag{7}$$

Unit cable costs (per metre), correction factors for cross-sectional area, and specific costs for substations (per MW) are taken from the detailed cost model developed in [7].

Installation costs C_{INST} depend on port distance and water depth, using port data from [30]. Only ports equipped with dry-dock facilities are considered, ensuring a minimum level of infrastructure for offshore-wind assembly, maintenance, and logistics. They include turbine and substructure installation, port-related activities, inter-array cable installation (scaled consistently with cable CAPEX), and mooring installation, assumed equal to 0.81 M€/MW. Offshore logistics are represented by a fixed cost of 2.6×10^{-3} M€/MW [27].

Contingency costs C_{CON} account for construction-phase uncertainties and are set to 0.275 M€/MW, consistent with values reported in the literature [27].

2.4.2. Decommissioning costs

Decommissioning costs are modelled as a fraction of the corresponding installation-related costs, reflecting a reverse installation process that is typically faster and less complex than the initial deployment. The fractions applied to the main cost categories are taken from [31]. In the LCOE and LCOH expressions, DECOM is added as a terminal cost at the end of the project lifetime.

Table 2
Vessel cost parameters used for O&M cost estimation.

Parameter		CTV	SOV/FSV	AHTS
Number of technicians	[-]	15	20	30
Cost per technician	[€ h^{-1}]	9.46	9.46	9.46
Charter cost	[€ h^{-1}]	150.25	1000	928.9
Fuel consumption	[€ h^{-1}]	154.87	190.34	538.69
Fuel consumption with load	[€ h^{-1}]	–	–	1000.13

Table 3
Maintenance-support infrastructure cost parameters per MW of installed capacity.

Component	Value [€ MW^{-1} yr^{-1}]
Ports and onshore logistics	1309
Substation maintenance	297.5
Export cable surveys and repairs	297.5
Array cable surveys and repairs	833
Scour and structural surveys	952
Lifting, climbing and safety equipment inspections	357
SCADA and condition monitoring	1428
SAP and marine coordination	1428
Weather forecasting	154.7
Administration	833
Insurance	15 000
Total	22889.7

2.4.3. Operational expenditures

Operational expenditures are divided into operational costs and maintenance support infrastructure costs, as detailed in SPOWIND deliverable [32]:

$$\mathrm{OPEX} = C_{\mathrm{op}} + C_{\mathrm{infr}}, \tag{8}$$

where C_{op} accounts for corrective and periodic maintenance, and C_{infr} includes port costs and non-turbine infrastructure (substations, cables, structures, and monitoring systems).

Operation costs are divided into corrective maintenance C_{CM} and periodic maintenance C_{PM}. Corrective maintenance requires SOV, AHTS, and CTV vessels, and is modelled as

$$C_{\mathrm{CM}} = t^{\mathrm{op}}_{\mathrm{SOV}} C_{\mathrm{SOV}} + t^{\mathrm{op}}_{\mathrm{AHTS}} C_{\mathrm{AHTS}} + t^{\mathrm{op}}_{\mathrm{AHTS,nl}} C_{\mathrm{AHTS,fuel,nl}} + t^{\mathrm{op}}_{\mathrm{AHTS,l}} C_{\mathrm{AHTS,fuel,l}}, \tag{9}$$

where vessel hourly and fuel costs are given in Table 2. The operating time for each vessel is

$$t^{\mathrm{op}} = N_t \left[N_i \left(\frac{2 d_{\mathrm{port}}}{V_{\mathrm{speed}}} \right) + t_{\mathrm{rep}} \right], \tag{10}$$

where N_t is the number of turbines, N_i the annual interventions per turbine, d_{port} the port distance, V_{speed} the vessel speed, and t_{rep} the on-site repair time. The main parameters used in Eq. (9) are summarised on Table A.1 and A.2 in Appendix. Periodic maintenance follows the same formulation but involves only CTV vessels. The vessel cost parameters (crew, charter, fuel consumption) used in this study are summarised in Table 2 [32].

Maintenance-support infrastructure costs C_{infr} cover onshore logistics, substation O&M, cable inspection and repair, structural and scour inspections, lifting and safety equipment, SCADA and condition monitoring, marine coordination, and insurance. These are modelled as fixed annual costs per MW of installed capacity (Table 3) (see Fig. 4).

2.4.4. LCOH formulation and additional hydrogen-related costs

The LCOH formulation extends the LCOE framework by including hydrogen-related CAPEX, OPEX, and decommissioning costs associated with the electrolyser, power converters, desalination unit, and transport

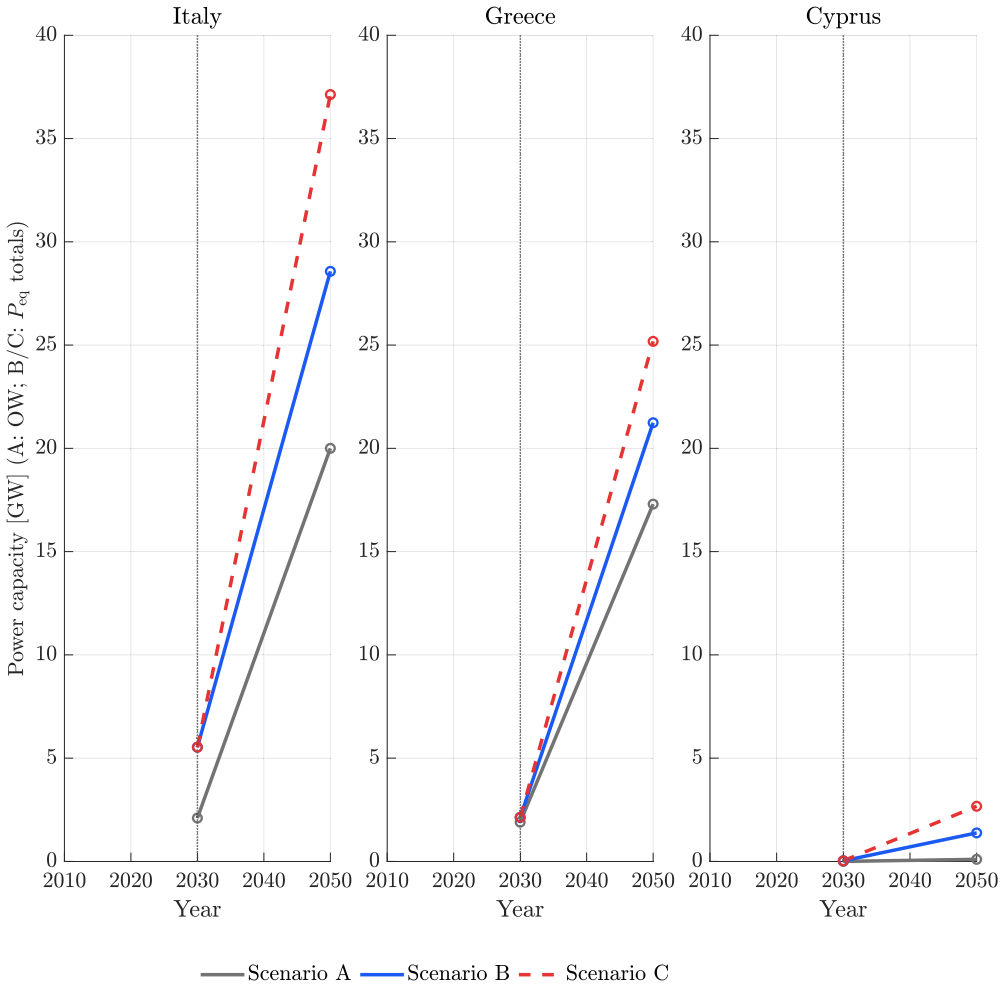


Fig. 4. Offshore wind and equivalent power requirements in Scenarios A–C for Italy, Greece, and Cyprus in 2030 and 2050. Grey solid lines show Scenario A (offshore wind only), blue solid lines Scenario B (offshore wind plus domestic hydrogen), and red dashed lines Scenario C (export-enhanced hydrogen, 2050 only).

system, denoted as CAPEX_H, OPEX_H and DECOM_H:

$$\begin{cases} \mathrm{CAPEX_H} = C_{\mathrm{el}} + C_{\mathrm{conv}} + C_{\mathrm{des}} + C_{tr}, \\ \mathrm{OPEX_H} = O_{\mathrm{el},y} + O_{\mathrm{conv},y} + O_{\mathrm{des},y} + O_{tr,y}, \\ \mathrm{DECOM_H} = D_{\mathrm{el}} + D_{\mathrm{conv}} + D_{\mathrm{des}} + D_{tr}, \end{cases} \tag{11}$$

where subscripts *el*, *conv*, *des* and *tr* refer to the electrolyser, converters, desalination, and transport systems, respectively. For centralised offshore configurations, hydrogen transport introduces an additional cost component C_{tr}. Both pipeline and ship-based transport are considered: pipelines are suitable for short distances, while ship transport becomes more economical at larger distances from shore. System sizing and transport cost modelling follow the SPOWIND project deliverable [33]. The electrolyser CAPEX is modelled as

$$C_{\mathrm{el}} = \mathrm{RC_{el}} P_{\mathrm{rat,el}} + N_s \mathrm{SC_{el}}, \tag{12}$$

where $P_{\mathrm{rat,el}}$ is the rated power of the electrolyser (kW), $\mathrm{RC_{el}}$ is the specific capital cost (€ $\mathrm{kW^{-1}}$), N_s is the number of replacements over the project lifetime, and $\mathrm{SC_{el}}$ is the cost of each replacement. The specific cost $\mathrm{RC_{el}}$ follows a learning-curve formulation:

$$\begin{cases} \mathrm{RC_{el}} = \left(k_0 + k P_{\mathrm{rat,el}}^{\alpha-1}\right) \left(\dfrac{Y}{Y_0}\right)^{\beta} + \mathrm{RC_0}, \\ \mathrm{SC_{el}} = 0.12 \left(\mathrm{RC_{el}} P_{\mathrm{rat,el}}\right), \end{cases} \tag{13}$$

Table 4
Cost parameters for the electrolysis system used in the CAPEX model [13].

Parameter	Value
k_0	673.73€
k	10876.93€
α	0.662
Y_0	2020
β	−0.445

where parameters are reported in Table 4, Y is the commissioning year, and $\mathrm{RC_0}$ is an additional fixed cost. In this study, $\mathrm{RC_0}$ is set to 300 € $\mathrm{kW^{-1}}$ and two replacements are assumed over 25 years.

The converter's CAPEX is given by

$$C_{\mathrm{conv}} = \mathrm{RC_{conv}} P_{\mathrm{rat,farm}} \mathrm{CF_{mean}}, \tag{14}$$

where RCconv is the specific converter cost and $P_{\mathrm{rat,farm}}$ the wind farm's rated power.

The desalination system CAPEX is modelled as

$$C_{\mathrm{des}} = \mathrm{RC_{des}} V_{\mathrm{H_2O}}, \tag{15}$$

where $\mathrm{RC_{des}}$ is the specific cost (1500 € $\mathrm{m^{-3}\,h^{-1}}$) and $V_{\mathrm{H_2O}}$ is the nominal water flow rate ($\mathrm{m^3\,h^{-1}}$). The desalination unit is sized at 80% of the electrolyser rated power, assuming a small freshwater buffer

Table 5
Offshore-wind targets and offshore-attributed green-hydrogen volumes for the three stylised scenarios in Italy, Greece, and Cyprus. Scenario A: offshore-wind capacity targets for electricity supply. Scenario B: 30% of the national green-hydrogen target supplied by offshore wind. Scenario C: 60% of the 2050 green-hydrogen target supplied by offshore wind (export-enhanced case). Hydrogen volumes M_{H_2} refer only to the offshore-attributed share.

Country	Year	Scenario A: OW		Scenario B: H_2 central (30%)			Scenario C: H_2 export (60%, 2050)		
		P_{OW} [GW]	Ref.	M_{H_2} [Mt yr^{-1}]	$P_{el,eq}$ [GW]	$P_{eq,B}$ [GW]	M_{H_2} [Mt yr^{-1}]	$P_{el,eq}$ [GW]	$P_{eq,C}$ [GW]
Italy	2030	2.1	[36]	0.60	3.43	5.53	–	–	–
	2050	20.0	[37]	1.50	8.57	28.57	3.00	17.13	37.13
Greece	2030	1.9	[38]	0.0405	0.23	2.13	–	–	–
	2050	17.3	[39]	0.69	3.94	21.24	1.38	7.88	25.18
Cyprus	2030	0.00	[40]	0.0045	0.03	0.03	–	–	–
	2050	0.10	[41]	0.225	1.28	1.38	0.45	2.57	2.67

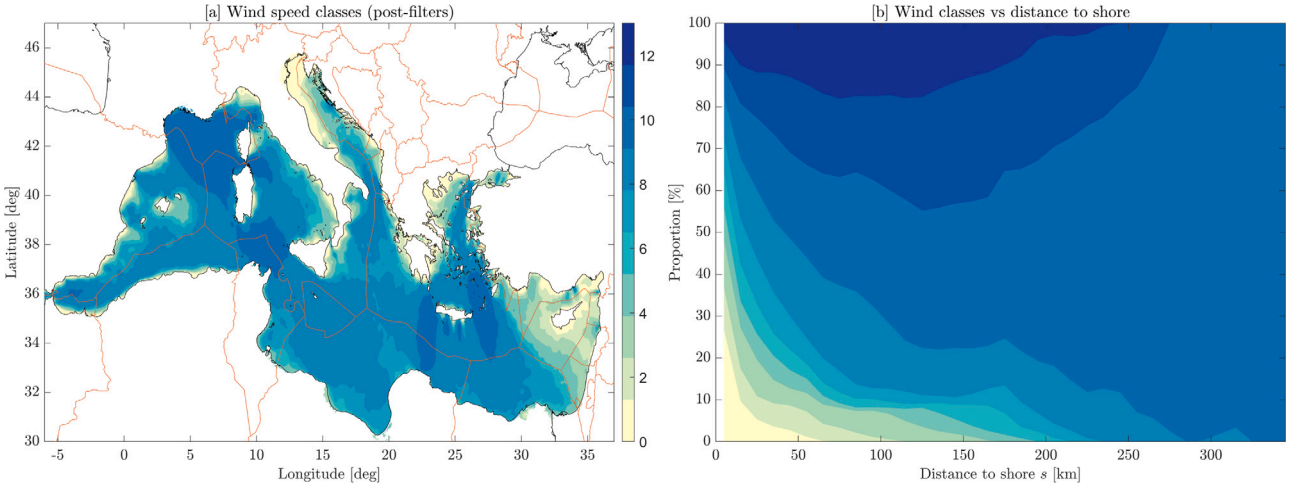


Fig. 5. Spatial distribution of the Mediterranean wind resource classified into wind speed classes over the entire basin (left) and wind speed distribution as a function of distance to shore (right).

tank. The nominal water flow rate is related to the electrolyser size by

$$V_{H_2O} = \dot{v}_{H_2O} \frac{0.8 P_{rat,el}}{1000}, \tag{16}$$

where $\dot{v}_{H_2O}$ is the specific water consumption, taken as 0.263 m^3 MWh^{-1}.

Annual OPEX for the hydrogen subsystem is modelled as a fixed fraction of the corresponding CAPEX:

$$\begin{cases} O_{el,y} = 0.015\, C_{el}, \\ O_{conv,y} = 0.015\, C_{conv}, \\ O_{des,y} = 0.040\, C_{des}, \end{cases} \tag{17}$$

and decommissioning costs are taken as a fraction of CAPEX, with percentages (2%) based on techno-economic studies of large-scale electrolysis systems [34,35].

The LCOH is then defined as

$$\mathrm{LCOH} = \frac{\mathrm{CAPEX} + \mathrm{CAPEX_H} + \sum_{i=1}^{n} \frac{\mathrm{OPEX} + \mathrm{OPEX_H}}{(1+r)^i} + \frac{\mathrm{DECOM} + \mathrm{DECOM_H}}{(1+r)^n}}{\sum_{i=1}^{n} \frac{\mathrm{AHP}_i}{(1+r)^i}}, \tag{18}$$

where r is the discount rate (equal to the WACC), n the project lifetime in years, and AHP_i the annual hydrogen production in years i.

2.4.5. Visual impact assessment

The visual impact of each offshore wind configuration is evaluated with a GIS-based method adapted from Maslov et al. [42]. Three location-dependent indices, horizon occupation, number of visible turbines and geometric alignment, are combined into a visual-impact score VI ranging from 0 (not visible) to 75 (maximum occupation with strong alignment). A set of 108 coastal observation points is defined along the Mediterranean, by intersecting heritage sites and population-density, following the SPOWIND methodology [32]. Their spatial distribution is shown in Fig. 6(b). The points provide a consistent basin-scale set of viewing locations for screening purposes, but do not constitute a statistically representative sample of Mediterranean social acceptance. For each point and candidate farm, VI is computed for viewing distances between 12 and 50 km and for all farm designs considered. Sites with $VI > 50$ at any observation point are classified as non-eligible, representing configurations unlikely to obtain social acceptance and planning consent. Although this approach does not explicitly account for local topography, atmospheric visibility conditions, cumulative visual effects, or empirically derived social-acceptance functions, it offers a consistent and computationally efficient screening criterion for basin-scale planning. The use of LCOE penalty classes enables visual sensitivity to be integrated directly into the techno-economic optimisation, allowing all Mediterranean grid cells and wind-farm configurations to be compared on a common basis while preserving the regional scope of the analysis.

For all sites that remain eligible after applying the $VI \leq 50$ mask (Section 2.4.5), the visual-impact score is translated into an economic penalty on the LCOE. The VI is discretised into four classes (0–10, 10–20, 20–30, and 30–50), to which LCOE multipliers of 0%, +2%, +5%, and +10% are assigned, respectively. This discretisation is inspired by the Saint-Nazaire case study of Maslov et al. [42], where the composite visual-impact operator is mapped into categorical

Table 6
Indicative optimal offshore wind farm configurations in Italy, Greece, and Cyprus, expressed as share of the eligible area [%]. A radial internal layout is selected at all locations, and all floating solutions adopt a TLP substructure; D denotes the rotor diameter.

Country	Wind farm type [%]		Optimal inter-turbine spacing [%]						
	Fixed-bottom	Floating	5D	7D	9D	11D	13D	15D	17D
Italy	0.31	99.69	0	0	0	0.29	0.27	63.70	35.75
Greece	2.46	97.55	0	0	0.01	2.24	7.99	66.55	23.21
Cyprus	0	100	0	0	0	0	0	1.15	98.85

classes ranging from negligible to very high impact to support planning decisions. In the present Mediterranean-wide application, the original classes are aggregated into broader bands and interpreted as visually acceptable ($VI < 10$), moderate impact ($10 \leq VI < 30$) and high impact ($VI \geq 30$).

The associated LCOE multipliers act as a stylised proxy for the additional costs and risks expected in increasingly sensitive visual settings, rather than as a detailed monetisation of social acceptance. For each grid cell and configuration, a penalised LCOE is thus obtained by applying the corresponding multiplier to the techno-economic LCOE. The optimal wind farm layout at each location is then selected by minimising this penalised LCOE, and the resulting configuration maps form the basis for the subsequent geospatial potential, supply-curve, and scenario-coverage analyses. The LCOE multipliers adopted here are not empirically established and are used as a transparent, stylised proxy for the additional costs and risks expected in visually sensitive settings. The approach should therefore be regarded as a preliminary screening criterion, aimed at introducing visual sensitivity into a basin-scale techno-economic optimisation in a consistent and reproducible way, rather than as a validated assessment of social acceptance.

2.5. National targets and scenario definition for offshore wind and green hydrogen

Following the approach of Putuhena et al. for the UK net-zero analysis [43], the long-term ambitions of Italy, Greece, and Cyprus are organised into three stylised scenarios, since these countries provide comparable and publicly available offshore-wind and green-hydrogen targets. Scenario A considers only offshore-wind deployment for electricity supply, using the offshore-wind capacity targets reported in national energy and offshore strategies. Scenario B assumes that offshore wind also contributes to domestic green-hydrogen production, supplying a fraction $\alpha_{OW} = 0.3$ (30%) of each national green-hydrogen target. Scenario C explores an export-enhanced 2050 case, with offshore wind providing $\alpha_{OW} = 0.6$ (60%) of the national green-hydrogen volume, in line with system-level studies that identify offshore wind as a major, though not exclusive, pillar of the future European hydrogen supply mix [44].

For each country c and scenario s, the hydrogen volume attributed to offshore wind is denoted $M_{H_2}^{(c,s)}$ [Mt yr^{-1}]. The associated equivalent continuous electrolysis power $P_{el,eq}^{(c,s)}$ [GW] is evaluated assuming a specific electricity consumption of 50 kWh kg^{-1} (1 Mt yr^{-1} $\approx$ 50 TWh yr^{-1} $\approx$ 5.71 GW) [44].

The total equivalent power requirement of the offshore wind-to-hydrogen system is

$$P_{eq}^{(c,s)} = P_{OW}^{(c,s)} + P_{el,eq}^{(c,s)}, \tag{19}$$

where $P_{OW}^{(c,s)}$ is the offshore-wind capacity target in Scenario A. In Scenario A, $P_{el,eq}^{(c,A)} = 0$ and thus $P_{eq}^{(c,A)} = P_{OW}^{(c,A)}$; in Scenarios B and C, $P_{eq}^{(c,s)}$ represents the combined offshore-wind and electrolysis capacity required to meet both electricity and offshore-attributed hydrogen demand.

Table 5 summarises the offshore-wind targets and offshore-attributed hydrogen volumes for Scenarios A–C. In Italy, Scenario B assigns 0.6 and 1.5 Mt,yr^{-1} of hydrogen to offshore wind in 2030 and 2050 (3.43 and 8.57 GW), corresponding to total equivalent capacities of 5.53 and 28.57 GW; Scenario C raises the 2050 offshore share to 3.0 Mt,yr^{-1} (17.13 GW), for a total equivalent requirement of 37.13 GW.

3. Results

3.1. Offshore wind resource in the mediterranean sea

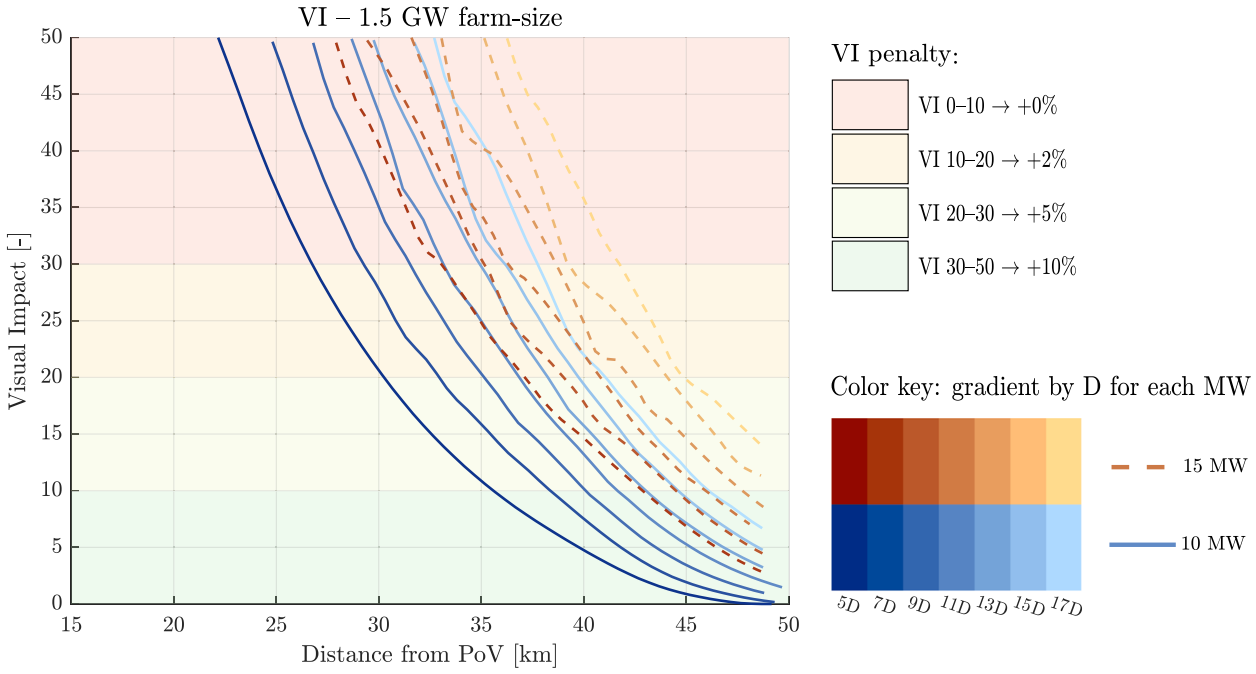
The presentation of results begins with a brief characterisation of the Mediterranean wind resource, as this underpins the subsequent techno-economic patterns. Fig. 5 reports the 20-year mean wind speed, with a basin-wide average of 8.3 m s^{-1} and a clear strengthening of the resource with increasing distance from the coast. This gradient anticipates that the most profitable offshore spot where the techno-economic analysis identifies the lowest LCOE and LCOH configurations. Higher resource levels generally occur at increasing distances from the coastline, as further shown in Fig. 5, which reports the resource distribution as a function of distance from shore. This trend indicates that the most favourable conditions are predominantly offshore, highlighting the relevance of deep water and floating deployment solutions. One of the key outputs of the analysis is the delineation of the eligible offshore area. After applying all MSP-related exclusion layers, the initially available Mediterranean sea space is reduced to 7.3 $\cdot 10^5$ km^2, corresponding to approximately 24.3%.

3.2. Technical potential and spatial LCOE and LCOH

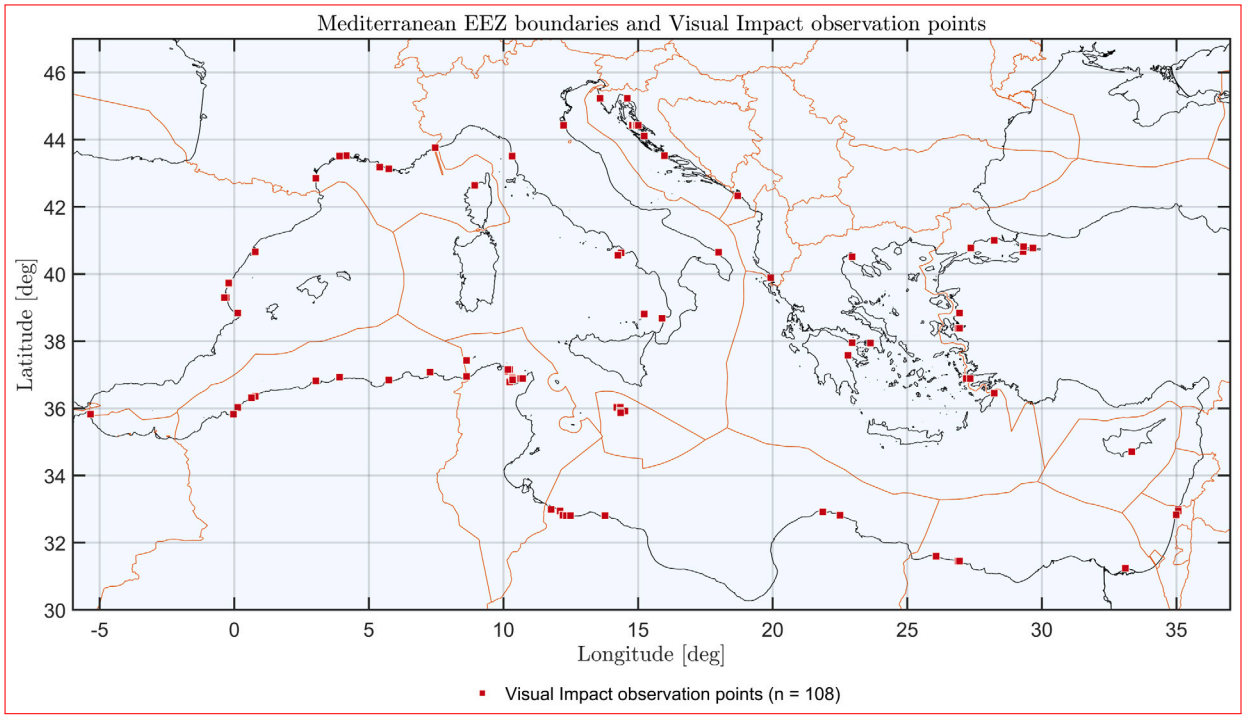
3.2.1. Optimal spatially resolved LCOE

Building on the identified eligible areas and resource conditions, the framework is applied to compute site-specific AEP and, where relevant, AHP for each candidate wind-farm layout. For each eligible grid cell, 378 configurations, combining turbine rating, substructure type, wind-farm size, internal electrical layout, and inter-turbine spacing, are simulated, yielding an LCOE and, for PtX configurations, the corresponding LCOH. The visual-impact score VI associated with each configuration is then converted into an LCOE multiplier, as described in Section 2.4.5, producing a single scalar objective: the penalised LCOE. The optimisation at the cell level is therefore not a multi-criteria ranking but a direct comparison of penalised LCOE values: for each grid cell, the configuration with the minimum penalised LCOE is selected as optimal. Fig. 6 presents a representative example for the 1.5 GW wind farm, illustrating the variation of the VI as a function of turbine size and spacing index. The results show that, for larger farm extensions, the visual impact increases with increasing spacing, reflecting the combined effect of a wider spatial footprint and enhanced visual exposure. The resulting maps provide the spatial distribution of optimal LCOE/LCOH and of the corresponding technology mix (turbine size, foundation type, spacing, and internal layout) used in the subsequent potential, supply-curve and scenario-coverage analyses.

Fig. 7 (above) shows the spatial distribution of the LCOE across the eligible area, with and without the visual impact penalities, where the optimisation leads to a quasi-unique selection of configurations at each location. As shown in Fig. 8, in regions suitable for monopile foundations, corresponding to the deployment of 10 MW wind turbines, the 1.5GW wind farm is consistently selected as the optimal solution.



(a) Example of visual-impact scores and associated penalty classes for different spacings of the 1.5 GW wind-farm configuration.



(b) Spatial distribution of the 108 coastal observation points used for visual-impact screening across the Mediterranean basin. EEZ boundaries are shown for geographical reference.

Fig. 6. Visual-impact screening framework: (a) visual-impact scores and associated penalty classes; (b) spatial distribution of the observation points used in the basin-scale analysis.

Conversely, in floating installation areas, the 0.99 GW wind farm coupled with a TLP is consistently identified as the optimal solution, as it provides the best trade-off between hydrodynamic interaction losses of the floating substructure and the associated costs, resulting in a lower overall cost than the other platforms. For example, at fixed bathymetry and distance to ports, the semi-submersible yields a specific overall cost of 1.22 M€ MW^{-1}, the spar 1.03 M€ MW^{-1}, while the TLP achieves the lowest value at 0.87 M€ MW^{-1}. Regarding the internal electrical layout, a radial configuration is selected for all analysed locations, as it requires a smaller expansion area for the farm and is the most economical option in terms of electrical infrastructure. Meanwhile, the optimal inter-turbine spacing varies spatially depending on the local wind resource. Fig. 7 (right) reports the spatial distribution of the selected spacing index, highlighting a decreasing trend with increasing

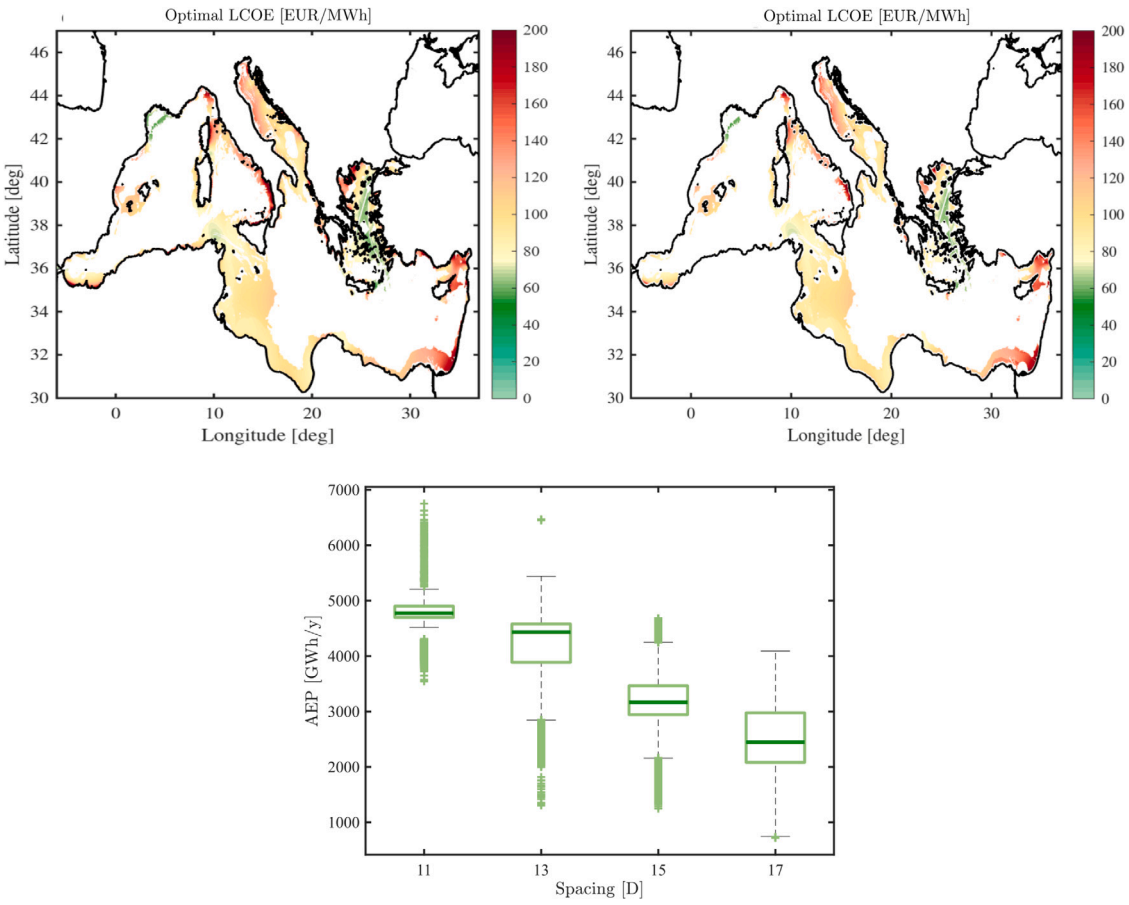


Fig. 7. Optimal LCOE without (left) and with (right) VI penalties, and AEP distribution for the optimal inter-turbine spacing (below). The eligible area decreases from $7.3 \cdot 10^5$ km^2 (24.25% of the Mediterranean EEZ domain) to $6.6 \cdot 10^5$ km^2 (21.96%) when the VI screening is applied; the country-level breakdown is reported in Table A.3.

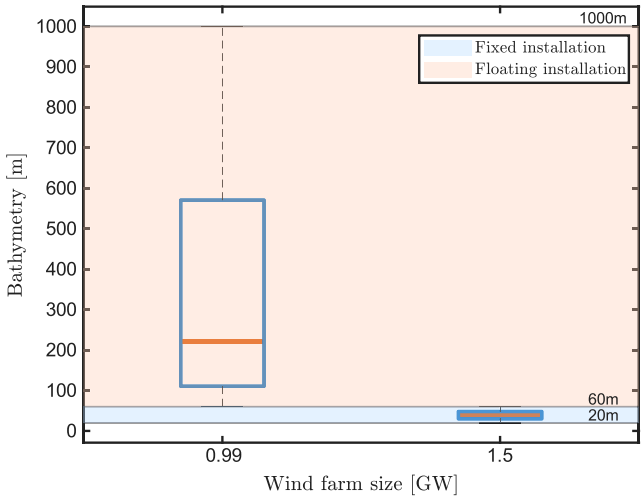


Fig. 8. Optimal size selection with respect to bathymetry level.

productivity. This indicates that more spatially extended wind farms are favoured in low-resource areas, where the relative impact of infrastructure costs and electrical losses becomes less significant compared to wake-induced energy losses. Table 6 summarises the optimal configurations in the three focus countries (radial layout and TLP substructure are selected throughout). Floating solutions cover almost the entire eligible area, while the optimal spacing concentrates on 15D in Italy and Greece and on 17D in Cyprus; Greece shows the broadest spacing distribution.

3.2.2. *Technical potential of the optimal solution*

Based on these eligible areas, the suitable offshore area and the associated technical potential are estimated for each country (Fig. 9). Aggregating across all Mediterranean offshore eligible areas, the total gross technical offshore wind potential amounts (computed using the Eq. (2)) to $2.56 \cdot 10^3$ TWh yr^{-1}, while the amount related to only European countries is $1.36 \cdot 10^3$ TWh yr^{-1}. The country-level results, summarised in Fig. 9, shows marked differences across the basin. Italy concentrates the largest share of suitable offshore area, with about $1.5 \cdot 10^5$ km^2 (roughly one fifth of the Mediterranean total) and therefore one of the highest national technical potentials.

Libya, although characterised by a smaller suitable footprint, attains the largest technical potential, reflecting particularly favourable wind and depth conditions within its eligible zones. Other countries, such as Greece, Spain, and Tunisia, occupy intermediate positions, combining more modest suitable areas with resource levels that still support sizeable offshore contributions to their long-term decarbonisation strategies.

3.2.3. *Optimal spatially resolved LCOH*

In parallel with the LCOE-based optimisation, spatially resolved maps of the LCOH for the centralised offshore hydrogen production scenario are presented in Fig. 10. The LCOH exhibits spatial trends consistent with those observed for the LCOE, reflecting the strong coupling between electricity generation and hydrogen production costs.

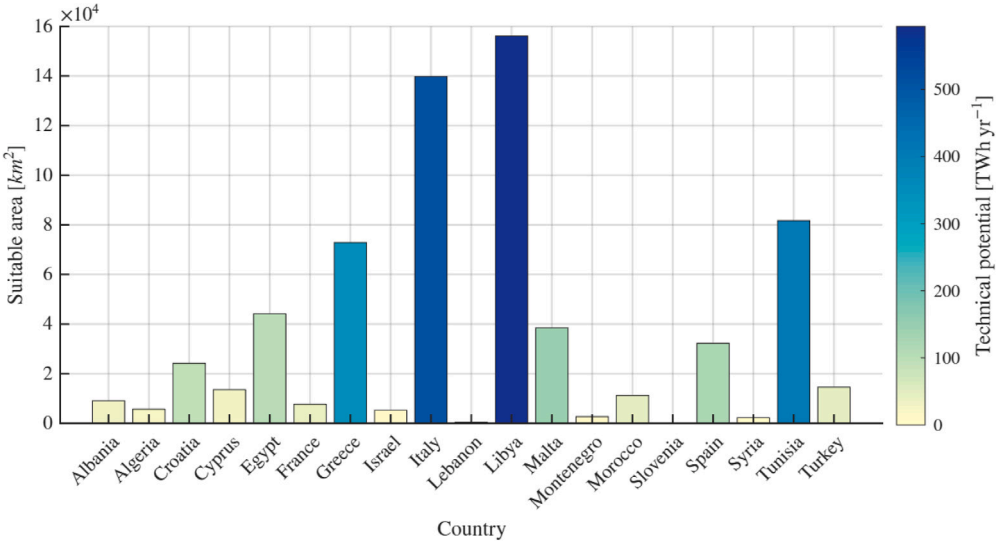


Fig. 9. Suitable area and technical potential for each country.

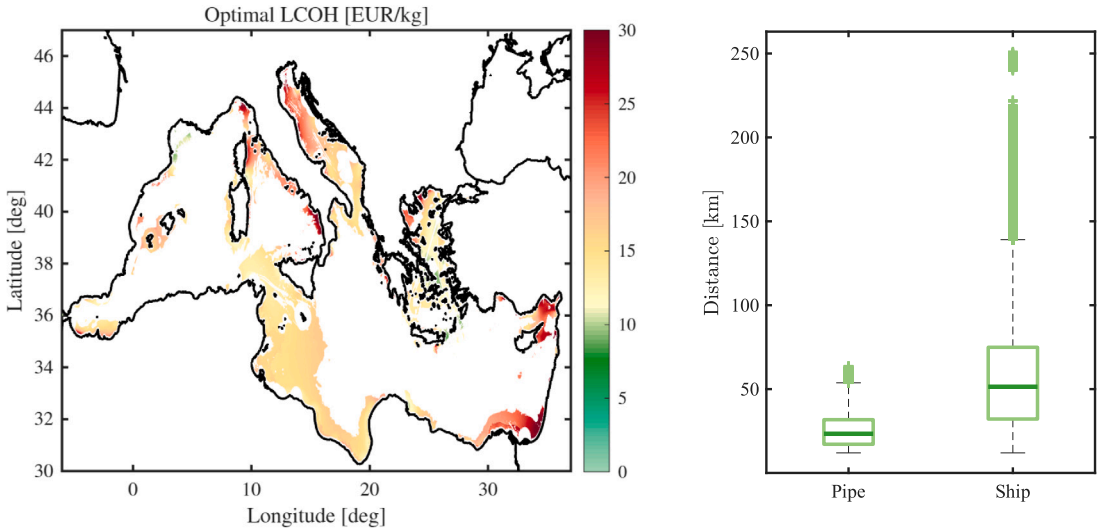


Fig. 10. Optimal LCOH and relative optimal transport type distance distribution.

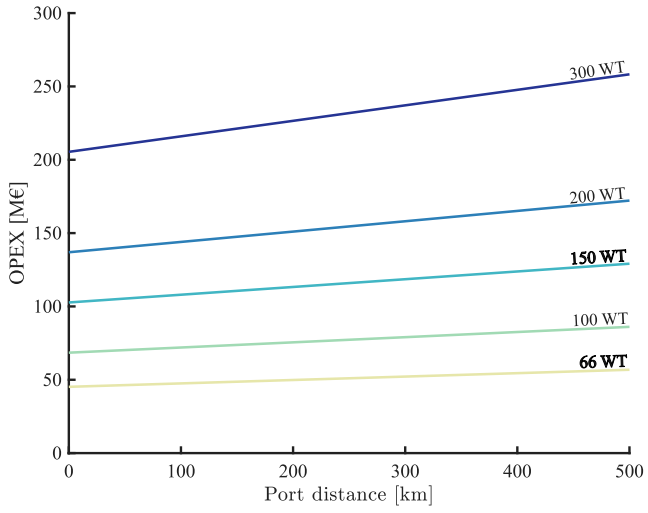


Fig. 11. Operational expenditure in M€ related to distance to ports.

In addition, as shown in Fig. 10 (right), the optimal hydrogen transport strategy to shore is identified: pipeline transport is preferred for offshore distances up to approximately 70 km, while shipping becomes economically favourable beyond this threshold due to the rapidly increasing costs associated with long-distance pipelines. In addition, the OPEX distribution with the distances is provided in (Fig. 11). OPEX is one of the most influential components of the economic results and is strongly affected by the distance from ports. The figure shows that both OPEX values and the slope of the curves increase with the number of wind turbines, indicating a growing sensitivity of operating costs to port distance for larger wind farm layouts.

3.3. Scenario coverage: offshore wind and hydrogen targets

The scenario-coverage assessment focuses on Italy, Greece, and Cyprus, which provide comparable and publicly available offshore-wind and green-hydrogen targets. Fig. 12 provides the geographical context for this selection, showing their EEZs and the final offshore areas available after the MSP and water-depth exclusions. The resulting available offshore area amounts to 139,705 km^2 in Italy, 72,780 km^2 in Greece, and 13,552 km^2 in Cyprus.

The techno-economic-geospatial results are linked to national deployment trajectories by quantifying, for each country and for Scenarios A–C, the fraction of required equivalent power supplied by offshore

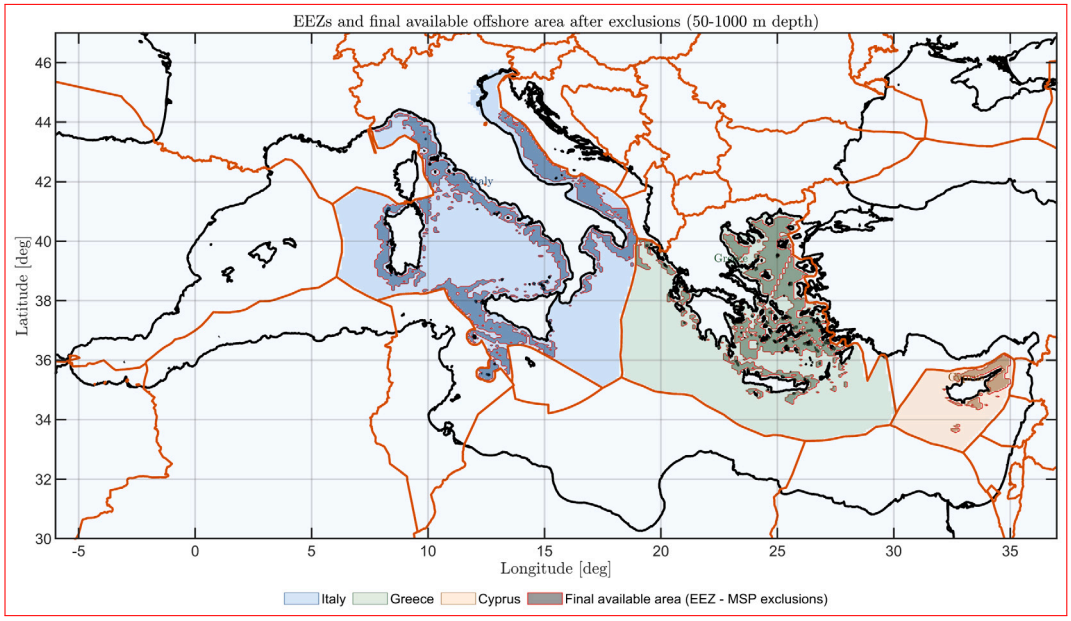


Fig. 12. Exclusive economic zones (EEZs) of Italy, Greece, and Cyprus and the final offshore areas available for analysis after marine spatial-planning (MSP) and water-depth exclusions (50–1000 m).

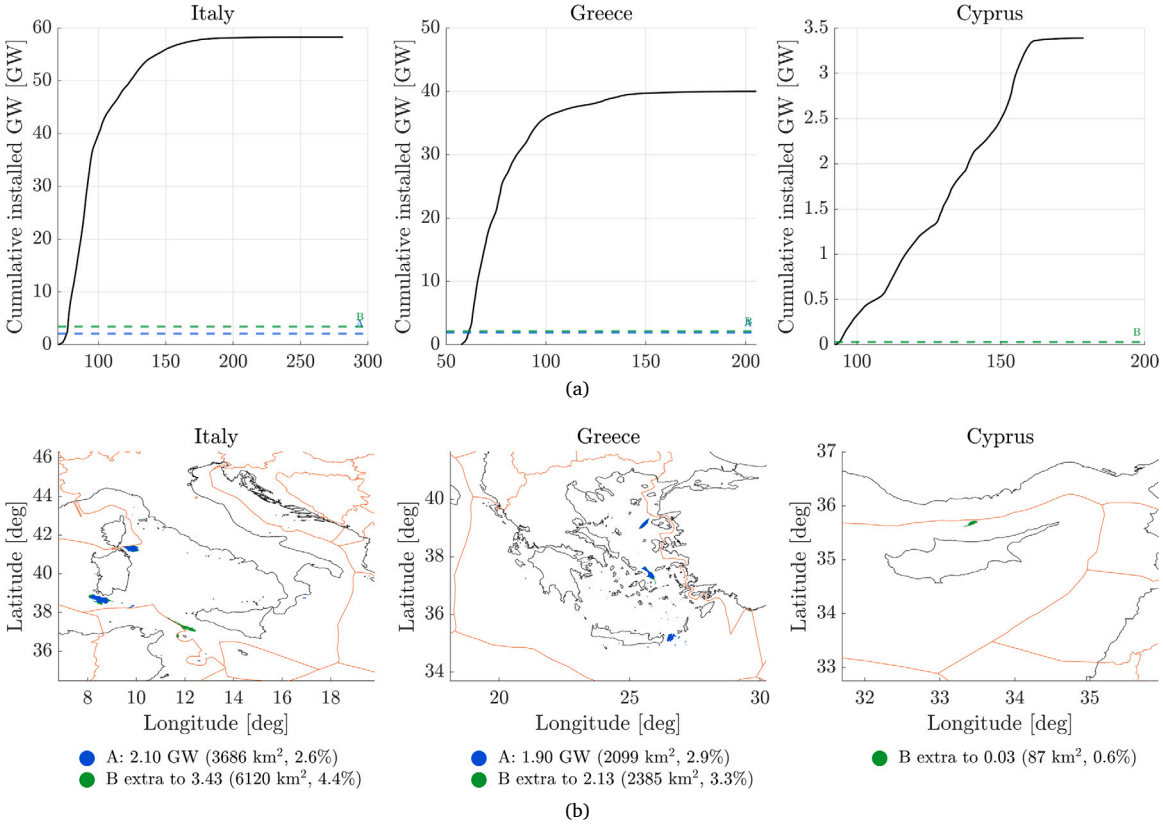


Fig. 13. (a) Cumulative 2030 supply curves for Italy, Greece, and Cyprus, with eligible sites ordered by LCOE and cumulative installed capacity; the horizontal lines indicate the Scenario A and Scenario B power requirements. (b) Lowest-LCOE areas selected in 2030 to meet Scenarios A and B in each country, illustrating the corresponding spatial footprint within the eligible offshore area.

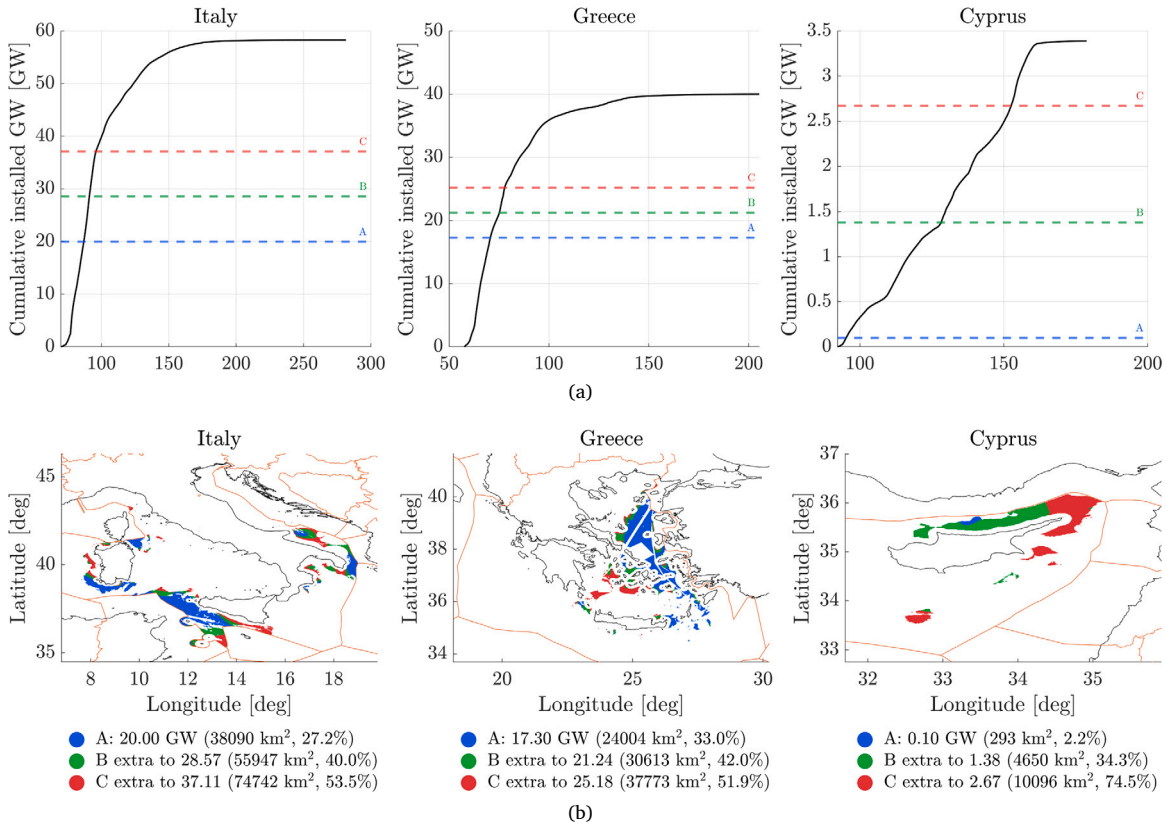


Fig. 14. (a) Cumulative 2050 supply curves for Italy, Greece, and Cyprus, with eligible sites ordered by LCOE and cumulative installed capacity; the horizontal lines indicate the Scenario A–C power requirements. (b) Lowest-LCOE areas selected in 2050 to meet Scenarios A–C in each country, highlighting the additional offshore area required when moving from electricity-only (A) to domestic hydrogen (B) and export-enhanced hydrogen supply (C).

wind and PtX, together with the corresponding utilisation of MSP- and VI-constrained offshore area. Eligible grid cells are ranked by increasing LCOE and aggregated into cumulative supply curves.

In 2030 (Fig. 13), Scenarios A and B are satisfied using only the lowest-LCOE offshore sites. Italy and Greece require less than about 8% of the eligible offshore area, while Cyprus remains below 1%, indicating that short-term deployment is not constrained by techno-economic potential or MSP-compatible sea space.

By 2050 (Fig. 14), the export-enhanced Scenario C substantially increases offshore area occupation and infrastructure requirements. The optimisation progressively expands towards deeper and more distant offshore regions, increasing the dependence on floating technologies and hydrogen transport systems. Occupied eligible area rises from 27% to 54% in Italy, from 33% to 52% in Greece, and from 2% to nearly 75% in Cyprus when moving from Scenario A to Scenario C.

For Italy, the results can be compared with the national development and grid-connection context. Medici et al. [45] identify 55 floating offshore wind projects submitted to the Italian permitting process, corresponding to a combined proposed capacity of 43.4 GW, and discuss their associated TERNA grid-connection context. This is comparable in scale with the 37.11 GW required by Scenario C in the present analysis, which occupies 74,742 km^2 (53.5%) of the Italian available offshore area. The project portfolio should be regarded as a development-reference layer, rather than as an availability mask; therefore, this comparison provides an order-of-magnitude consistency check rather than a polygon-level validation.

For Greece, the nationally designated development areas and the basin-scale technical screening address different planning questions. The Greek National Development Programme identifies 1196.85 km^2 of medium-term development areas, within a wider national programme covering 2712 km^2 [46]. In contrast, the Mediterranean-scale technical assessment of Faraggiana et al. [7], which applies a distinct set of spatial and techno-economic constraints, reports 32,378 km^2 of suitable floating offshore area for Greece. The 72,780 km^2 obtained in the present study should therefore be interpreted as a basin-scale technical envelope, rather than as a projection of nationally designated development space.

3.4. Cross-country comparison and policy implications

Fig. 15 summarises avoided CO_2-equivalent emissions from substituting grey hydrogen with offshore-wind hydrogen in Scenarios B and C. Avoided emissions are calculated as $(EF_{\mathrm{grey}} - EF_{\mathrm{green}})M_{\mathrm{H_2,selected}}$, using 9.5 and 0.5 $\mathrm{kgCO_2eq\,kgH_2^{-1}}$ for grey and wind-based hydrogen, respectively. Thus, $M_{\mathrm{H_2,selected}}$ [$\mathrm{MtH_2\,yr^{-1}}$] is multiplied by 9.0 to obtain $\mathrm{MtCO_2eq\,yr^{-1}}$. The factors are consistent in magnitude with the LCA pathway values reported by Hydrogen Council and LBST [47]; this comparative indicator excludes site-specific transport emissions and is not a project-specific net LCA. In 2030, avoided emissions remain below 1 $\mathrm{MtCO_2\,yr^{-1}}$ in Greece and Cyprus, while Italy already reaches several $\mathrm{MtCO_2\,yr^{-1}}$ due to its larger hydrogen target and offshore potential. By 2050, Scenario B leads to avoided emissions on the order of tens of $\mathrm{MtCO_2\,yr^{-1}}$ in Italy and around 10 $\mathrm{MtCO_2\,yr^{-1}}$ in Greece, while Cyprus

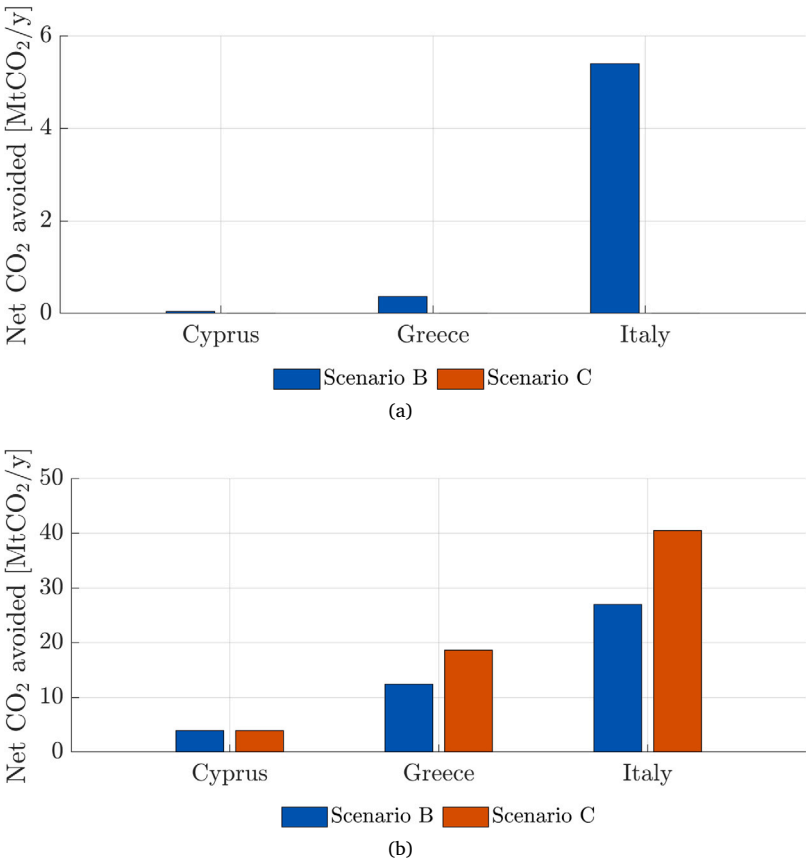


Fig. 15. Avoided CO_2-equivalent emissions from offshore-wind hydrogen in Scenarios B (domestic supply) and C (export-enhanced) for the three focus countries. Panel (a) shows the 2030 values, panel (b) the 2050 values.

reaches a few $MtCO_2\,yr^{-1}$ despite its smaller system size. Moving from Scenario B to the export-enhanced Scenario C increases avoided emissions by approximately 40%–60% in all countries. Overall, the results indicate that Mediterranean offshore wind and PtX systems can provide substantial contributions to long-term decarbonisation targets, although increasing hydrogen penetration progressively shifts deployment towards offshore regions associated with higher infrastructure costs and stronger spatial constraints.

4. Discussion

4.1. Mediterranean offshore potential in the context of previous assessments

After applying MSP and visual-impact constraints, approximately $6.6 \cdot 10^5$ km^2 remain eligible for offshore wind deployment, corresponding to a gross technical potential of $2.56 \cdot 10^3$ $TWh\,yr^{-1}$. The cell-by-cell assessment yields a technically installable nominal capacity substantially above the 90–125 GW deployment potential reported for 2050 in the European Commission Mediterranean offshore-grid study [8]. This contrast indicates that, after MSP and visual screening, resource availability is not the limiting factor; deployment is primarily governed by grid integration and cross-border planning. Compared with the floating-only assessment by Faraggiana et al. [7], the present analysis confirms Libya, Tunisia, Italy, and Greece as the dominant high-potential regions, while highlighting a progressive shift of the techno-economic optimum towards deeper floating areas characterised by higher wind-resource availability.

4.2. Optimal layouts and visual constraints

The optimisation over 378 configurations per grid cell, spanning turbine rating, foundation, farm scale, topology, and spacing, reveals consistent spatial trends between wind resource, layout density, and infrastructure costs. Dense layouts are favoured in high-resource regions, where wake losses dominate over electrical-infrastructure costs, whereas larger spacing is selected in lower-resource areas to reduce wake interactions. Radial internal electrical layouts are systematically preferred over star and double-ring topologies, indicating that the additional redundancy of more complex networks does not compensate for the associated CAPEX increase under Mediterranean conditions. High LCOE values are mainly associated with the simultaneous occurrence of deep-water deployment, long export distances, and strong visual-impact penalties. The inclusion of VI-based penalties modifies the spatial techno-economic optimum, particularly in near-shore regions with favourable infrastructure accessibility. Although simplified, the adopted penalty formulation indicates that visual constraints can significantly affect the distribution of competitive offshore sites in densely populated Mediterranean coastal areas.

4.3. Offshore wind-to-hydrogen chains and national strategies

In 2030, both electricity-only (Scenario A) and electricity–hydrogen (Scenario B) deployment targets are achieved using only the lowest-LCOE offshore sites, requiring less than 8% of the eligible offshore

Table A.1
Vessels assigned for each maintenance task (major repairs and replacements).

Component	Major	Repl.	Component	Major	Repl.
Pitch/Hyd	SOV/FSV	SOV/FSV	Hub	SOV/FSV	SOV/FSV
Other components	SOV/FSV	SOV/FSV	Heaters/coolers	SOV/FSV	–
Generator	SOV/FSV	AHTS	Yaw system	SOV/FSV	SOV/FSV
Gearbox	SOV/FSV	AHTS	Tower/foundation	SOV/FSV	–
Blades	SOV/FSV	AHTS	Power supply/converter	SOV/FSV	SOV/FSV
Grease/oil/cooling liq.	SOV/FSV	–	Service items	SOV/FSV	–
Electrical components	SOV/FSV	SOV/FSV	Transformer	SOV/FSV	SOV/FSV
Contactor/c.b./relay	SOV/FSV	SOV/FSV	Floating platform (semi-sub)	–	AHTS
Controls	SOV/FSV	SOV/FSV	Mooring lines	–	SOV/FSV
Safety	SOV/FSV	–	Anchors	–	SOV/FSV
Sensors	SOV/FSV	–	Power cable (interarray)	–	SOV/FSV
Pumps/motors	SOV/FSV	–	Export cable	–	SOV/FSV

area in Italy and Greece, and below 1% in Cyprus. Under these conditions, deployment is not constrained by techno-economic potential or MSP-compatible sea space. By 2050, the export-enhanced Scenario C substantially increases spatial occupation and infrastructure requirements, progressively shifting deployment towards deeper and more distant offshore regions. Consequently, occupied eligible area rises to approximately 54% in Italy, 52% in Greece, and nearly 75% in Cyprus. The results highlight a progressive trade-off between additional CO_2 abatement and offshore spatial occupation, with marginal hydrogen expansion increasingly relying on sites associated with higher infrastructure costs and stronger spatial constraints.

5. Conclusion

This study introduced a Mediterranean-wide framework that couples MSP-constrained geospatial screening, high-resolution offshore wind and hydrogen simulations, detailed farm and grid design, and levelised cost metrics for electricity and hydrogen. The framework links basin-scale resource and constraint mapping with national offshore wind and green-hydrogen trajectories for Italy, Greece, and Cyprus. After applying marine spatial-planning and visual-acceptance constraints, about $6.6 \cdot 10^6$ km^2 of sea space (roughly one quarter of the basin) remains eligible for offshore wind, corresponding to a gross technical potential of several terawatts and approximately $2.56 \cdot 10^3$ $TWh\,yr^{-1}$ of electricity. Within this envelope, the optimisation systematically favours large bottom-fixed farms in shallow waters and 0.99 GW floating configurations in deeper zones, with radial internal layouts and spacing that tightens where wind resources are strongest. Visual-impact penalties reallocate capacity away from the most sensitive coastal cells while preserving the lowest-LCOE clusters. For the three focus countries, techno-economic potential is not a binding constraint. In 2030, electricity-only and combined electricity–hydrogen scenarios can be met using a small share of the eligible area; by 2050, even export-enhanced hydrogen pathways remain feasible but require substantial fractions of constrained sea space and yield CO_2 abatements of several tens of $MtCO_2\,yr^{-1}$. These results indicate that offshore wind and PtX can become structural components of Mediterranean net-zero strategies, while also underscoring the need for coordinated MSP, grid, and port planning and hydrogen-corridor design.

Further work should investigate the sensitivity of the results to wind-resource assumptions, including sub-hourly variability, site-specific wind shear, technical availability, and uncertainty propagation to AEP, LCOE, and LCOH. It should also refine visual and ecological constraints, extend the analysis to additional countries and PtX vectors, and couple the geospatial results with power-system and hydrogen-network models. Main limitations include the literature-based WACC and cost-reduction factors, adopted without a dedicated sensitivity analysis, and the LCOE-based allocation of hydrogen sites; both will be addressed in future work.

CRediT authorship contribution statement

Ermando Petracca: Writing – review & editing, Writing – original draft, Visualization, Validation, Software, Project administration, Methodology, Investigation, Formal analysis, Data curation, Conceptualization. **Viola De Clerck:** Writing – review & editing, Writing – original draft, Visualization, Validation, Software, Methodology, Investigation, Formal analysis, Data curation, Conceptualization. **Emiliano Gorr-Pozzi:** Writing – review & editing, Writing – original draft, Validation, Supervision, Software, Methodology, Investigation, Formal analysis, Data curation, Conceptualization. **Gabriele Mangia:** Writing – review & editing, Visualization, Validation, Software, Methodology, Investigation, Formal analysis, Data curation. **Farhan Haider Joyo:** Writing – review & editing, Writing – original draft, Visualization, Software, Methodology, Investigation, Formal analysis, Data curation. **João Francisco Marques:** Writing – review & editing, Visualization, Software, Methodology, Investigation, Formal analysis, Data curation. **Giovanni Bracco:** Writing – review & editing, Project administration, Funding acquisition.

Declaration of competing interest

The authors declare that they have no known competing financial interests or personal relationships that could have appeared to influence the work reported in this paper.

Acknowledgements & funding

This work was carried out in the framework of the SPOWIND - Spatial Planning for Offshore WIND Industry Development project, supported by the Interreg Euro-MED Programme (Euro-MED0200199 – SPOWIND). The authors gratefully acknowledge the project partners and data providers for access to metocean datasets, GIS layers, and the techno-economic assumptions used in this study. The authors express their gratitude for the funds received from the Ministry of University and Research and PNRR's PhD scholarship program, defined in DM-352/2022 in collaboration with Eni S.p.A. This publication is part of the PNRR-NGEU project.

Appendix. Operation and maintenance assumptions

See Tables A.1–A.3.

Table A.2
Average material costs, operational hours and number of site visits for replacement and major repairs of 15 MW floating turbines over a 25-year period [48–50]. Superscripts: (i) equal to 1% of floater cost per maintenance; (ii) uses AHTS vessels instead of SOV.

Component	Failure rate [yr^{-1}]	Repair price [€]	Repair time [h]	Cost per turbine [€]	Hours of operations [h]	Site visits [-]
Pitch/Hyd	0.001	1248999.02	24	31224.98	0.60	0.025
Other components	0.001	10 000	24	250	0.60	0.025
Generator	0.095	1062505.56	20	2523450.71	47.50	(ii)
Gearbox	0.154	3131951.24	24	12058012.28	92.40	(ii)
Blades	0.001	13076771.36	16	326919.28	0.40	(ii)
Grease/oil/cooling liq.	0	0	0	0	0	0
Electrical components	0.002	824450.57	18	41222.53	0.90	0.050
Contactor/c.b./relay	0.002	13 500	24	675	1.20	0.050
Controls	0.001	13 000	12	325	0.30	0.025
Safety	0	0	0	0	0	0
Sensors	0	0	0	0	0	0
Pumps/motors	0	0	0	0	0	0
Hub	0.001	605792.33	24	15144.81	0.60	0.025
Heaters/coolers	0	0	0	0	0	0
Yaw system	0.001	941676.30	24	23541.91	0.60	0.025
Tower/foundation	0	0	0	0	0	0
Power supply/converter	0.005	1049559.57	24	131194.95	3.00	0.125
Service items	0	0	0	0	0	0
Transformer	0.001	70 000	24	1750	0.60	0.025
Floating platform	0.21	(i)	12	(i)	63.00	(ii)
Mooring lines	0.12	45 000	12	135054.02	36.01	3.00
Anchors	0.107	82 500	12	219882.73	31.98	2.67
Power cable (interarray)	0.0000323	–	12	–	–	–
Export cable	0.167	–	24	–	–	–

Table A.3
Country-level eligible offshore area within the Mediterranean EEZs, before and after the visual-impact (VI) screening. Percentages refer to the EEZ area of each country.

Country	EEZ area [km^2]	Eligible area without VI [km^2]	[%]	Eligible area with VI [km^2]	[%]
Albania	13,422	9165	68.28	9059	67.49
Algeria	157,555	9288	5.90	5688	3.61
Croatia	57,213	30,648	53.57	24,193	42.29
Cyprus	122,270	15,401	12.60	13,552	11.08
Egypt	217,852	50,559	23.21	44,131	20.26
France	96,829	10,990	11.35	7690	7.94
Greece	578,617	74,881	12.94	72,780	12.58
Israel	32,702	6615	20.23	5275	16.13
Italy	622,358	149,083	23.95	139,705	22.45
Lebanon	23,320	672	2.88	459	1.97
Libya	453,323	166,998	36.84	156,127	34.44
Malta	64,999	45,610	70.17	38,486	59.21
Montenegro	6922	4348	62.81	2681	38.73
Morocco	21,797	12,183	55.89	11,249	51.61
Slovenia	174	0	0.00	0	0.00
Spain	306,220	37,020	12.09	32,210	10.52
Syria	12,458	2228	17.88	2228	17.88
Tunisia	119,811	88,773	74.09	81,687	68.18
Turkey	106,041	16,317	15.39	14,566	13.74
Total	3013,883	730,779	24.25	661,766	21.96

References

[1] S. Bouckaert, C. McGlade, A. Fernandez Pales, U. Remme, Net zero by 2050: A roadmap for the global energy sector, 2021, Paris, October 2021. URL https://www.iea.org/reports/net-zero-by-2050.

[2] E. Faraggiana, A. Ghigo, M. Sirigu, E. Petracca, G. Giorgi, G. Mattiazzo, G. Bracco, Optimal floating offshore wind farms for mediterranean islands, Renew. Energy 221 (2024) 119785, http://dx.doi.org/10.1016/j.renene.2023.119785, URL https://www.sciencedirect.com/science/article/pii/S0960148123017007.

[3] D. Quint, J.K. Lundquist, D. Rosencrans, Simulations suggest offshore wind farms modify low-level jets, Wind. Energy Sci. 10 (1) (2025) 117–142, http://dx.doi.org/10.5194/wes-10-117-2025.

[4] Y. Wang, G. Dong, J. Yu, C. Qin, Y. Feng, Y. Deng, M. Zhang, In-situ green hydrogen production from offshore wind farms, a prospective review, Renew. Energy 239 (2025) 122099, http://dx.doi.org/10.1016/j.renene.2024.122099, URL https://www.sciencedirect.com/science/article/pii/S0960148124021670.

[5] J. Lloret, et al., Unravelling the ecological impacts of large-scale offshore wind farms in the Mediterranean Sea, Sci. Total Environ. 824 (2022) 153803, http://dx.doi.org/10.1016/j.scitotenv.2022.153803.

[6] A. Martinez, G. Iglesias, Evaluation of offshore wind energy zones within marine spatial planning: A case study in the Spanish Mediterranean Sea, Energy Rep. 11 (2024) 3461–3473, http://dx.doi.org/10.1016/j.egyr.2024.03.018.

[7] E. Faraggiana, A. Ghigo, M. Sirigu, E. Petracca, G. Giorgi, G. Mattiazzo, Floating offshore wind potential for Mediterranean countries, Heliyon 10 (13) (2024) e33948, http://dx.doi.org/10.1016/j.heliyon.2024.e33948.

[8] Guidehouse, Study on the Offshore Grid Potential in the Mediterranean Region, Tech. Rep., (ENER/2018/OP/0005) European Commission, Directorate-General for Energy, 2020, http://dx.doi.org/10.2833/742284, URL https://data.europa.eu/doi/10.2833/742284.

[9] L. Serri, D. Airoldi, F. Lanni, R. Naldi, A. Castorrini, F. Rispoli, T. Soukissian, L. Castro-Santos, M. Le Boulluec, C. Maisondieu, Technical and economic challenges for floating offshore wind deployment in Italy and in the Mediterranean Sea, Wiley Interdiscip. Rev.: Energy Environ. 13 (4) (2024) e533, http://dx.doi.org/10.1002/wene.533.

[10] P. Gkeka-Serpetsidaki, S. Papadopoulos, T. Tsoutsos, Assessment of the visual impact of offshore wind farms, Renew. Energy 190 (2022) 358–370, http://dx.doi.org/10.1016/j.renene.2022.03.091, URL https://www.sciencedirect.com/science/article/pii/S0960148122003755.

[11] R. Travaglini, F. Superchi, F. Lanni, G. Manzini, L. Serri, A. Bianchini, Towards the development of offshore wind farms in the Mediterranean Sea: A techno-economic analysis including green hydrogen production during curtailments, IET Renew. Power Gener. 18 (18) (2024) 3112–3126, http://dx.doi.org/10.1049/rpg2.13135.

[12] H. Jiang, L. Xiong, W. Chen, D. Geng, B. Xu, Economic comparison of offshore wind-to-hydrogen production routes based on a unit energy transmission assessment model, Front. Energy Res. 13 (2025) 1709439, http://dx.doi.org/10.3389/fenrg.2025.1709439.

[13] V. De Clerck, E. Petracca, F.H. Joyo, A. Bacan, G. Mangia, C. Nikolakakos, G. Radulovic, J.F. Marques, A. Dimeas, D. Groppi, D.A. Garcia, G.U. Magni, E. Gorr-Pozzi, G. Bracco, From wind to hydrogen: mapping the competitiveness of hybrid offshore configurations in the Mediterranean Sea, Front. Energy Res. Volume 14 - 2026 (2026) http://dx.doi.org/10.3389/fenrg.2026.1765111, URL https://www.frontiersin.org/journals/energy-research/articles/10.3389/fenrg.2026.1765111.

[14] European Marine Observation and Data Network (EMODnet), EMODnet human activities, maritime boundaries and sea uses GIS layers, 2024, Online GIS database, available via EMODnet portal: spatial data on marine uses, protected areas and maritime boundaries.

[15] GEBCO Compilation Group, The GEBCO 2023 grid – A continuous terrain model of the global oceans and land, 2023, General Bathymetric Chart of the Oceans (GEBCO) digital bathymetric model, available from the British Oceanographic Data Centre (BODC).

[16] C. Bak, F. Zahle, R. Bitsche, T. Kim, A. Yde, L.C. Henriksen, M.H. Hansen, J.P.A.A. Blasques, M. Gaunaa, A. Natarajan, The DTU 10-MW reference wind turbine, in: Danish Wind Power Research 2013, 2013.

[17] E. Gaertner, J. Rinker, L. Sethuraman, F. Zahle, B. Anderson, G.E. Barter, N.J. Abbas, F. Meng, P. Bortolotti, W. Skrzypinski, et al., IEA Wind TCP Task 37: Definition of the IEA 15-Megawatt Offshore Reference Wind Turbine, Tech. Rep., National Renewable Energy Lab.(NREL), Golden, CO (United States), 2020.

[18] MOREnergylab, MOST: Matlab for offshore simulation tool, 2025, https://github.com/MOREnergylab/MOST.
[19] S. Schimanke, M. Ridal, P. Le Moigne, L. Berggren, P. Undén, R. Randriamampianina, U. Andréa, E. Bazile, A. Bertelsen, P. Brousseau, P. Dahlgren, L. Edvinsson, A. El Said, M. Glinton, S. Hopsch, L. Isaksson, R. Mladek, E. Olsson, A. Verrelle, Z.Q. Wang, CERRA sub-daily regional reanalysis data for europe on single levels from 1984 to present, 2021, http://dx.doi.org/10.24381/cds.622a565a, Copernicus Climate Change Service (C3S), Climate Data Store.
[20] J.V. Taboada, V. Diaz-Casas, X. Yu, Reliability and maintenance management analysis on offshore wind turbines (OWTs), Energies 14 (22) (2021) 7662, http://dx.doi.org/10.3390/en14227662.
[21] K. Zeng, D. Zhang, Recent progress in alkaline water electrolysis for hydrogen production and applications, Prog. Energy Combust. Sci. 36 (3) (2010) 307–326, http://dx.doi.org/10.1016/j.pecs.2009.11.002, Comparative discussion of alkaline and PEM electrolysers, efficiencies, dynamics and costs.
[22] O. Schmidt, A. Gambhir, I. Staffell, A. Hawkes, J. Nelson, S. Few, Future cost and performance of water electrolysis: An expert elicitation study, Int. J. Hydrog. Energy 42 (52) (2017) 30470–30492, http://dx.doi.org/10.1016/j.ijhydene.2017.10.045, Provides system-level efficiency and performance metrics usable to derive surrogate efficiency curves.
[23] B. Lee, L. Wang, Z. Wang, N. Cooper, M. Elimelech, Directing the research agenda on water and energy technologies with process and economic analysis, Energy & Environ. Sci. 16 (2023) http://dx.doi.org/10.1039/D2EE03271F.
[24] International Energy Agency, Global energy and climate model documentation 2024, 2024, https://www.iea.org.
[25] E. Tapoglou, G.L. Mc, A. Georgakaki, A. Mountraki, S. Letout, E. Ince, B.J. Gea, A. Schmitz, M. Grabowska, et al., Clean energy technology observatory: Wind energy in the European union-2025 status report on technology development, trends, value chains and markets, 2023.
[26] R. Wiser, J. Rand, J. Seel, P. Beiter, E. Baker, E. Lantz, P. Gilman, Expert elicitation survey predicts 37% to 49% declines in wind energy costs by 2050, Nat. Energy 6 (5) (2021) 555–565, http://dx.doi.org/10.1038/s41560-021-00810-z.
[27] Guide to a floating offshore wind farm, 2025, Online; https://guidetofloatingoffshorewind.com/. (Accessed 25 April 2025).
[28] T. Ashuri, M.B. Zaaijer, J.R. Martins, J. Zhang, Multidisciplinary design optimization of large wind turbines—Technical, economic, and design challenges, Energy Convers. Manage. 123 (2016) 56–70.
[29] H. Díaz, C.G. Soares, Cost and financial evaluation model for the design of floating offshore wind farms, Ocean Eng. 287 (2023) 115841.
[30] Sea route & distance, http://ports.com.
[31] A. Myhr, C. Bjerkseter, A. Ågotnes, T.A. Nygaard, Levelised cost of energy for offshore floating wind turbines in a life cycle perspective, Renew. Energy 66 (2014) 714–728.
[32] SPOWIND Consortium, Techno-Economic Assessment Methods for Offshore Wind Farms, Tech. Rep., (Deliverable D2.3.1) SPOWIND – Spatial Planning for Offshore WIND Industry Development, Interreg Euro-MED, 2025, Publicly available project deliverable. URL https://spowind.interreg-euro-med.eu/wp-content/uploads/sites/42/techno-economic-assessment-methods-for-offshore-wind-farms_dlv.2.3.1_2.pdf.
[33] SPOWIND Consortium, Power-to-X Technologies and Opportunities, Tech. Rep., (Deliverable D3.2.1) SPOWIND – Spatial Planning for Offshore WIND Industry Development, Interreg Euro-MED, 2025, Publicly available project deliverable. URL https://spowind.interreg-euro-med.eu/wp-content/uploads/sites/42/power-to-x-technologies-and-opportunities_dlv-3.2.1_2.pdf.
[34] U. Caldera, C. Breyer, Learning curve for seawater reverse osmosis desalination plants: Capital cost trend of the past, present, and future, Water Resour. Res. 53 (12) (2017) 10523–10538, http://dx.doi.org/10.1002/2017WR021402.
[35] M. Papapetrou, A. Cipollina, U. La Commare, G. Micale, G. Zaragoza, G. Kosmadakis, Assessment of methodologies and data used to calculate desalination costs, Desalination 419 (2017) 8–19, http://dx.doi.org/10.1016/j.desal.2017.05.038.
[36] European Commission, Assessment of the Draft Updated Integrated National Energy and Climate Plan of Italy 2021–2030, European Commission, Directorate-General for Energy, 2023, Staff Working Document SWD(2023) — Assessment of Italy's draft updated NECP, Includes updated 2030 wind and offshore-wind capacity targets.
[37] C. Carraro, P. Criqui, et al., Achieving net zero emissions in Italy by 2050, Energies 15 (1) (2022) 46, http://dx.doi.org/10.3390/en15010046, Provides long-term decarbonisation scenarios for the Italian energy system.
[38] Hellenic Republic, Ministry of Environment and Energy, Draft Updated National Energy and Climate Plan 2021–2030 – Greece, Ministry of Environment and Energy, Athens, Greece, 2023, Includes updated targets for wind, offshore wind and electrolysers.
[39] Hellenic Hydrocarbons and Energy Resources Management Company (HEREMA), National Offshore Wind Farm Development Programme, HEREMA, Athens, Greece, 2023, Defines organised development areas and mid-/long-term offshore wind capacities for Greece.
[40] Republic of Cyprus, Ministry of Energy, Commerce and Industry, Cyprus' National Energy and Climate Plan 2021–2030 – Final Updated Version, Ministry of Energy, Commerce and Industry, Nicosia, Cyprus, 2024, Updated NECP including renewable and wind capacity trajectories.
[41] European Commission, EU Strategy to Harness the Potential of Offshore Renewable Energy for a Climate Neutral Future, European Commission, Brussels, Belgium, 2020, Presents indicative offshore wind and ocean-energy deployment targets to 2050.
[42] N. Maslov, C. Claramunt, T. Wang, T. Tang, Method to estimate the visual impact of an offshore wind farm, Appl. Energy 204 (2017) 1422–1430, http://dx.doi.org/10.1016/j.apenergy.2017.05.053.
[43] H. Putuhena, D. White, S. Gourvenec, F. Sturt, Finding space for offshore wind to support net zero: A methodology to assess spatial constraints and future scenarios, illustrated by a UK case study, Renew. Sustain. Energy Rev. 182 (2023) 113358, http://dx.doi.org/10.1016/j.rser.2023.113358, URL https://www.sciencedirect.com/science/article/pii/S1364032123002150.
[44] Clean Hydrogen Joint Undertaking, Strategic Research and Innovation Agenda 2021–2027, Clean Hydrogen JU, Brussels, Belgium, 2021, Reports state-of-the-art and target specific electricity consumption for electrolysers (around 50 kWh kg^{-1} H_2).
[45] D. Medici, A. Tonna, A. Segalini, Exploring future production scenarios for Italian offshore wind power, Wind. Energy Sci. 11 (2) (2026) 723–735, http://dx.doi.org/10.5194/wes-11-723-2026.
[46] T. Soukissian, N.-E. Koutri, F. Karathanasi, K. Kardakaris, A. Stefatos, A preliminary assessment of offshore winds at the potential organized development areas of the Greek seas using CERRA dataset, J. Mar. Sci. Eng. 13 (8) (2025) 1486, http://dx.doi.org/10.3390/jmse13081486.
[47] Hydrogen Council and Ludwig-Bolkow-Systemtechnik (LBST), Hydrogen Decarbonization Pathways: A Life-Cycle Assessment, Hydrogen Council, 2021, URL https://hydrogencouncil.com/wp-content/uploads/2021/01/Hydrogen-Council-Report_Decarbonization-Pathways_Part-1-Lifecycle-Assessment.pdf.
[48] J. Carroll, A. McDonald, D. McMillan, Failure rate, repair time and unscheduled O&M cost analysis of offshore wind turbines, Wind. Energy 19 (6) (2016) 1107–1119, http://dx.doi.org/10.1002/we.1887.
[49] T. Elusakin, M. Shafiee, T. Adedipe, F. Dinmohammadi, A stochastic Petri net model for O&M planning of floating offshore wind turbines, Energies 14 (2021) 1134, http://dx.doi.org/10.3390/en14041134.
[50] T. Ashuri, M.B. Zaaijer, J.R.R.A. Martins, J. Zhang, Multidisciplinary design optimization of large wind turbines: Technical, economic, and design challenges, Energy Convers. Manage. 123 (2016) 56–70, http://dx.doi.org/10.1016/j.enconman.2016.06.004.